GRADUATION THESIS

TRABAJO DE FIN DE GRADO

Numerical modeling of magnetosonic shocks: the Boris correction

---

by
Óscar Soler Pérez

Supervisor
Fernando Moreno Insertis

University of La Laguna

Physics Degree

July, 2023

Agradecimientos

Quisiera expresar mi más sincero agradecimiento a todas aquellas personas que han hecho posible el desarrollo de este trabajo. En primer lugar, deseo agradecer a mi tutor, Fernando Moreno Insertis, por su guía y orientación a lo largo de todo el proceso. Por compartir su conocimiento, forma de pensar y su tiempo, muchas gracias.

Mi agradecimiento se extiende a todas las personas que confiaron y me acompañaron durante estos meses de duro trabajo. A mi familia, por estar siempre ahí. A los compañeros de biblioteca, por amenizar las largas jornadas. A mis amigos, por motivarme a dar lo mejor de mí. Gracias.

Abstract

Advanced numerical methods are necessary to carry out simulations of magnetized fluids due to the highly non-linear nature of their equations. The timestep in the numerical calculation is inversely proportional to the speed of propagation of signals in the system, and it dangerously decreases when that speed is very large (like the Alfvén speed in the solar corona), sometimes rendering the calculation very difficult or just impossible. A solution to this problem, proposed by Boris 1970 and used in recent 3D models of the Sun (Rempel 2016, Cheung et al. 2019, Chen et al. 2022) includes extra terms in the magnetohydrodynamic (MHD) fluid equations that are disregarded in the standard MHD case, reducing the speed of propagation of signals. Additionally, the speed of light is artificially lowered. In this thesis, a numerical code is built from scratch and used to perform simulations of a 1D system with longitudinal velocity and transverse magnetic field. The code is used to study the semi-relativistic MHD case of the Boris correction, artificially changing the speed of light with a view to understanding whether this technique modifies the physics obtained in the model for the evolution of the magnetized fluid. It is concluded that the use of the Boris correction leads to an important decrease of the speed of propagation of shocks while increasing the jumps of the physical quantities across the shock. This leaves various open questions concerning the applicability of the Boris correction to explosive situations, whose analysis goes beyond the scope of the present Graduation thesis.

Resumen

El uso de métodos numéricos avanzados es imprescindible para el desarrollo de simulaciones de fluidos magnetizados debido a la naturaleza no lineal de sus ecuaciones. El paso temporal en los cálculos numéricos es inversamente proporcional a la velocidad de transmisión de información del sistema, decreciendo peligrosamente cuando esta velocidad es muy alta (como la velocidad de Alfvén en la corona solar) haciendo los cálculos imposibles en algunos casos. Una solución para este problema, propuesta por Boris 1970 y usada en modelos 3D recientes del sol (Rempel 2016, Cheung et al. 2019, Chen et al. 2022), incluye términos en las ecuaciones magnetohidrodinámicas (MHD) de los fluidos que son despreciados en el tratamiento MHD estándar, ralentizando la velocidad de transmisión de información. Adicionalmente, la velocidad de la luz se reduce de forma artificial. En este trabajo se construye un código numérico desde cero y se utiliza para realizar simulaciones unidimensionales de un fluido con velocidad longitudinal y campo magnético transversal. Usando dicho código se estudia el caso semi-relativista de la corrección de Boris, reduciendo artificialmente la velocidad de la luz con vistas a comprender si dicha técnica modifica la física obtenida en la evolución del fluido magnetizado. Se concluye que el uso de la corrección de Boris disminuye de forma importante la velocidad de propagación de los choques al tiempo que aumentan los saltos de las cantidades físicas a través del choque. Esto deja abiertas varias cuestiones sobre la aplicabilidad de la corrección de Boris en situaciones explosivas cuyo análisis escapa del objetivo del presente Trabajo de Fin de Grado.

Contents

1 Introduction

En la presente sección se expone la relevancia de los métodos numéricos en dinámica de fluidos. Se explica la corrección de Boris, técnica empleada para aumentar el paso temporal en los cálculos numéricos y usada actualmente en simulaciones en la corona solar. Se establece el método de comprobación de los efectos de esta técnica en la física resultante de las simulaciones numéricas.

Posteriormente se enumeran los objetivos de este trabajo. La construcción de un código para realizar simulaciones de dinámica de fluidos compresibles, extensión al caso de fluidos magnetizados con tratamiento semi-relativista y tests de la corrección de Boris mediante reducción artificial de la velocidad de la luz.

Finalmente se establece la metodología de este trabajo. Se especifica el uso de métodos numéricos, abordando los diferentes esquemas numéricos empleados y técnicas para reducir el ruido numérico.

The use of advanced numerical methods is necessary to understand the time evolution of magnetized fluids in the cosmos and of fusion plasmas, due to the highly non-linear nature of their governing equations. The *Computational Fluid Dynamics* (CFD) branch of Fluid Dynamics studies how to obtain those numerical solutions in a reliable and efficient manner. It is part of the state of the art in numerical modelling, and it has experienced a large boost in the past several decades thanks to the fast advance in supercomupting facilities.

In Astrophysics, in particular, the systems to model can be very inhomogeneous, leading to different evolutionary time scales in the different regions of the studied domain. In order to guarantee numerical stability, the standard numerical codes have to fulfill a condition, known as the Courant-Friedrichs-Lewy criterion (Courant et al. 1967, Laney 1998, Toro 2009), which imposes a maximum timestep for the numerical advance of the calculation which is inversely proportional to the speed of signal propagation in the physical system. In fact, the condition stipulates that $\Delta t < f_{CFL} \cdot \Delta x / v_{sign}$, with Δt and Δx the temporal and spatial resolution of the code; v_{sign} the signal propagation speed; and f_{CFL} a number of order unity. The fastest signal propagation speed in standard fluids interacting with electromagnetic fields (MHD fluids) is the magnetosonic speed, $\sqrt{c_s^2 + v_A^2}$, where c_s is the sound speed and v_A the Alfvén speed. Its non-relativistic expression is $v_A = B/\sqrt{\mu_0 \rho}$, where B, μ_0 and ρ denote the magnetic field, magnetic permeability of free space and plasma density. In low density regions the Alfvén speed can be very large. That is the case of the solar corona. The Alfvén speed is much greater than the sound speed there, and can be extremely large above active regions. If the spatial resolution

is fixed and the system has large Alfvén speeds, the timestep can become very small, rendering the numerical calculation very difficult or simply impossible to carry out.

A solution to this problem was proposed by Boris 1970 and is known as the *Boris correction*. This technique maintains the non-relativistic equations for the fluid, but, different to the standard MHD case, does not neglect the displacement-current term in Maxwell's equations. Therefore, a semi-relativistic set of MHD equations is obtained (see also Gombosi et al. 2002). Additionally, the speed of light is artificially lowered which reduces the speed of propagation of signals in the system (as detailed in this work). Although developed half a century ago, this method is being used nowadays in the recent simulations of the solar corona using the MURAM code (Rempel 2016, Cheung et al. 2019, Chen et al. 2022).

The general aim of this project is to create a code from scratch, written in the python programming language, that can solve the equations of compressible fluid dynamics in one spatial dimension with longitudinal velocity. The code is then enlarged to solve the MHD equations, also for a 1D system with longitudinal velocity but with transverse magnetic field, i.e., with the magnetic vector perpendicular to the direction of motion. In either case, the code is thoroughly tested for standard problems of wave and shock front propagation. Then the semi-relativistic case is studied, with a view to understanding whether the Boris correction does not modify the physics obtained in the model so that it can be used to calculate the evolution of the magnetized fluid. In the first part of the thesis, the non-relativistic equations for a non-magnetized ideal fluid are presented (Section 2), along with the numerical scheme used to build the code that solves them and the corresponding tests for cases with analytical solution. In Section 3, the non-relativistic MHD equations are derived; the numerical scheme is modified correspondingly and extensively tested for cases with analytical solution. The semi-relativistic magnetohydrodynamic equations for a one-dimensional case with longitudinal fluid motion perpendicular to the magnetic field are then presented in Section 4. The Boris correction is studied in Section 4.2; the tests to this approximation are explained in Section 4.4 using for them an initial column-like profile as is often used in the context of the standard Riemann problem of fluid mechanics. The final section summarizes the conclusions reached in this work.

1.1 Objectives

- Construction of a python code to solve the general equations of compressible fluid mechanics for a one-dimensional situation in the particular case of an ideal gas without heat conduction or viscosity and with longitudinal velocity only. Associated tests of propagation of (a) linear sound waves and (b) moderate to strong sonic shock fronts.

- Enlargement of the code to cope with the one-dimensional MHD problem of a magnetized fluid with magnetic field transverse to the direction of motion. Associated tests for (a) linear magnetosonic waves and (b) moderate to strong magnetosonic shocks.
- Extension of the code to deal with the one-dimensional semi-relativistic MHD problem. Associated tests for (a) linear semi-relativistic magnetosonic waves and (b) solution of the Riemann problem. Determination of the properties of the generated semi-relativistic magnetosonic shocks.
- Implementation of the Boris correction to artificially reduce the speed of light. Study of changes of the physical properties of the solution through (a) magnetosonic waves and (b) solution of the Riemann problem.

1.2 Methodology

This Graduation Thesis uses numerical methods to solve the fluid equations, indispensable because of the non-linear nature of the equations. They are discretized in space and time, substituting the space and time derivatives with finite differences. The choice of the finite difference scheme is a decisive part of the different numerical methods historically developed to solve this problem. We will use two different explicit numerical methods based on (a) the Lax-Friedrichs scheme and (b) the first-generation scheme known as MacCormack method, belonging to the Lax-Wendroff family of schemes. When testing the numerical results using cases with analytical solution, the Lax-Wendroff scheme is chosen because it is less dissipative than the Lax-Friedrichs scheme. Updating the code to cope with each set of equations, the hydrodynamic, magnetohydrodynamic and semi-relativistic magnetohydrodynamic cases are solved with the same numerical scheme.

Further to the numerical scheme, two methods are used to prevent numerical ringing when calculating the evolution of sharp transitions like shock fronts or contact discontinuities:
(a) to treat the shock front transition, an artificial viscosity is required to avoid unwanted unwanted numerical noise. In this thesis, the classical Richtmyer-Von Neumann artificial viscosity is used, which does a very good job at resolving the shock front with a chosen number of grid points. This artificial viscosity is designed so that it works in situations in which the fluid is being strongly compressed, like, precisely, across shocks.
(b) for the numerical ringing appearing around contact discontinuities (which are non-compressive), a 4^{th}-order filtering technique is used, as explained in Section 4.4.2.

2 Classical ideal fluid

En el presente capítulo se presentan las ecuaciones que describen la dinámica de un fluido clásico ideal. Se simplifica el sistema de ecuaciones para el caso unidimensional, en el que se desarrolla la teoría de ondas de sonido y de choques. Posteriormente se plantea la solución numérica que se seguirá para resolver las ecuaciones no lineales del sistema, se prueba con dos esquemas numéricos diferentes y se llevan a cabo tests para comprobar la efectividad del código resolviendo ondas de sonido y choques.

2.1 Equations

In order to obtain the set of semi-relativistic equations of magnetohydrodynamics, the simplest case is analyzed first. We start by writing the equations for a classical ideal fluid in the absence of gravity or electromagnetic field. Ideal here means that no dissipative phenomena are included, like heat conduction or viscosity.

2.1.1 Fully non-linear equations of a simple fluid

The equations that govern the evolution of the simplest compressible fluid can be written in explicit conservation form as follows:

$$\begin{cases} \dfrac{\partial \rho}{\partial t} = -\mathbf{div}(\rho\,\mathbf{v}) \ , & (2.1) \\ \dfrac{\partial}{\partial t}(\rho\,\mathbf{v}) = -\mathbf{div}(\rho\,\mathbf{v}\otimes\mathbf{v} + p\,\hat{\mathbf{I}}) \ , & (2.2) \\ \dfrac{\partial}{\partial t}\left(\rho\,\epsilon + \rho\dfrac{v^2}{2}\right) = -\mathbf{div}\left[\left(\rho\,\epsilon + \rho\dfrac{v^2}{2} + p\right)\mathbf{v}\right] \ , & (2.3) \end{cases}$$

where the six variables ρ, $\mathbf{v} = (v_x, v_y, v_z)$, p and ϵ denote the mass density per unit volume, fluid velocity, gas pressure and internal energy density per unit mass, respectively. Equations (2.1) through (2.3) are known as the continuity, momentum and energy equations. On the left hand side we find the volumetric densities, namely mass $u_m = \rho$, momentum $u_c = \rho\,\mathbf{v}$ and total energy $u_e = \rho\,\epsilon + \rho\,v^2/2$. On the right hand side there are the corresponding fluxes, namely the mass flux vector $\mathcal{F}_m = \rho\,\mathbf{v}$, the momentum flux tensor $\hat{\Pi} = \rho\,\mathbf{v}\otimes\mathbf{v} + p\,\hat{\mathbf{I}}$ and the total energy flux vector $\mathcal{F}_e = (\rho\,\epsilon + \rho\,v^2/2 + p)\,\mathbf{v}$.

These equations can also be written in terms of the Lagrange derivative, which provides

the change in time measured if one pursued the fluid element as it moves in space:

$$\begin{cases} \dfrac{D\rho}{Dt} = -\rho \, \mathbf{div}\, \mathbf{v} \ , & (2.4) \\ \rho \dfrac{D\mathbf{v}}{Dt} = -\nabla p \ , & (2.5) \\ \rho \dfrac{D\epsilon}{Dt} = -p \, \mathbf{div}\, \mathbf{v} \ . & (2.6) \end{cases}$$

The simulation experiments that will be carried out in this Graduation Thesis will focus on the one-dimensional case $\rho = \rho(x),\ \mathbf{v} = v(x)\,\mathbf{e_x},\ p = p(x)$. The system of equations (2.1-2.3) is then rewritten as:

$$\begin{cases} \dfrac{\partial \rho}{\partial t} = -\dfrac{\partial}{\partial x}(\rho v) \ , & (2.7) \\ \dfrac{\partial}{\partial t}(\rho v) = -\dfrac{\partial}{\partial x}\left(\rho v^2 + p\right) \ , & (2.8) \\ \dfrac{\partial}{\partial t}\left(\rho\epsilon + \rho\dfrac{v^2}{2}\right) = -\dfrac{\partial}{\partial x}\left[\left(\rho\epsilon + \rho\dfrac{v^2}{2} + p\right) v\right] \ . & (2.9) \end{cases}$$

Assuming that the fluid is an ideal gas, the following expression of the internal energy density can be used: $\rho\epsilon = \frac{p}{\gamma - 1}$. This provides a system of three non-linear equations and three variables.

2.1.2 Sound waves

Sound waves (also known as *pressure waves*) are the fundamental mode of propagation of small amplitude perturbations in a fluid. The basic equations are obtained by considering a fluid in static and stationary equilibrium extending to infinity with uniform values for the density ρ_{eq} and pressure p_{eq}. This equilibrium state trivially fulfills the basic equations (2.7-2.9). On top of this equilibrium, a perturbation is added with values $(\rho',\ v',\ p')$. If the perturbation is small, equations (2.7-2.9) can be expanded as a power series in the perturbations, keeping terms up to first order and disregarding all higher order terms i.e., neglecting non-linear effects. The equations obtained are:

$$\begin{cases} \dfrac{\partial}{\partial t}\left(\dfrac{\rho'}{\rho_{eq}}\right) = -c_{seq}\, \dfrac{\partial}{\partial x}\left(\dfrac{v'}{c_{seq}}\right) \ , & (2.10) \\ \dfrac{\partial}{\partial t}\left(\dfrac{v'}{c_{seq}}\right) = -\dfrac{c_{seq}}{\gamma}\, \dfrac{\partial}{\partial x}\left(\dfrac{p'}{p_{eq}}\right) \ , & (2.11) \\ \dfrac{\partial}{\partial t}\left(\dfrac{p'}{p_{eq}}\right) = -\gamma\, c_{seq}\, \dfrac{\partial}{\partial x}\left(\dfrac{\mathbf{v}'}{c_{seq}}\right) \ , & (2.12) \end{cases}$$

with γ the adiabatic index of the ideal gas and $c_{seq} = \sqrt{\gamma\, p_{eq}/\rho_{eq}}$ the sound speed calculated for the equilibrium values. For a single Fourier mode with frequency ω and wave number k, the previous equations imply the following dispersion relation: $\omega = \pm c_{seq}\, k$. The phase speed will

consequently be $v_{ph} = c_{seq}$, which is independent of k, so sound waves are non-dispersive. As all modes propagate with the same phase velocities, any initial small-amplitude perturbation with an arbitrary shape will shift in time without deformation in the direction of k with phase velocity v_{ph}.

If the study is restricted to the case of adiabatic perturbations, the amplitude relations of the perturbations are: $\frac{\rho'}{\rho_{eq}} = \frac{1}{\gamma}\frac{p'}{p_{eq}} = \pm\frac{v'}{c_{seq}}$. The density and pressure perturbations are in phase, while the velocity perturbation can be in phase or antiphase, depending on the direction of propagation.

2.1.3 Shocks

A different kind of perturbation propagation in fluids are shock waves. These are sharp transitions in the physical quantities of the fluid: density, pressure, temperature... One encounters shock fronts throughout the whole Universe, and in many situations on Earth as well. Shocks are a clear example of the effect of the non-linear terms of the equations, as they take relevance when the small perturbation conditions are not fulfilled.

To study the simplest case of one-dimensional shock propagation, one makes three assumptions. First, the shock profile is taken to have a step function shape, with all variables homogeneous in the pre and postshock regions. Secondly, the shock front is a plane advancing at constant speed V_{sh} in the x direction and, in that frame of reference, the system is assumed to be stationary (no time dependence). Finally, the shock is studied in that frame of reference moving with it. We shall call $u = v - V_{sh}$ the velocity of fluid elements relative to the shock front. Through mass, momentum and energy conservation considerations, the Rankine-Hugoniot jump conditions are derived:

$$\rho_1\, u_1 = \rho_0\, u_0 \ , \tag{2.13}$$

$$\rho_1\, u_1^2 + p_1 = \rho_0\, u_0^2 + p_0 \ , \tag{2.14}$$

$$\frac{u_1^2}{2} + \epsilon_1(\rho_1, p_1) + \frac{p_1}{\rho_1} = \frac{u_0^2}{2} + \epsilon_0(\rho_0, p_0) + \frac{p_0}{\rho_0} \ , \tag{2.15}$$

where the subscript 1 denotes the postshock values, and 0 denotes the preshock values. These two regions can be distinguished because the specific entropy of the postshock region is always greater than the preshock specific entropy. This is an important consequence of the nature of the equation of the entropy; this equation cannot be written in standard conservation form as $\frac{\partial u}{\partial t} = -\frac{\partial f(u)}{\partial x}$; rather, it has two added terms, which are always positive and are, therefore, entropy sources. In a real fluid, these terms are due to the dissipation associated with heat conduction and viscosity, which are irreversible processes and non-negligible across the shock

transition.

Substituting the internal energy density by its expression in terms of ρ and p for the simplest ideal gas, the different jumps p_1/p_0 and ρ_1/ρ_0 can be calculated in terms of the Mach number $M_0 = \frac{|u_0|}{c_{s0}}$:

$$\frac{p_1}{p_0} = \frac{2\gamma}{\gamma+1}M_0^2 - \frac{\gamma-1}{\gamma+1} , \tag{2.16}$$

$$\frac{\rho_0}{\rho_1} = \frac{2}{\gamma+1}\frac{1}{M_0^2} + \frac{\gamma-1}{\gamma+1} , \tag{2.17}$$

$$M_1^2 = \frac{2+(\gamma-1)M_0^2}{2\gamma M_0^2 - (\gamma-1)} . \tag{2.18}$$

These analytical relations will be used to ensure the proper functioning of the code developed in this thesis.

2.2 Numerical solution

Due to the highly non-linear behaviour of the system of equations that describe the fluid motion (2.1-2.3) or (2.7-2.9), exact analytical solutions are generally very difficult or simply impossible to obtain. A method involving numerical analysis has to be applied in order to solve the equations. The branch of Fluid Dynamics that studies how to obtain numerical solutions of the fluid equations is known as *Computational Fluid Dynamics* (CFD). It is part of the state of the art in numerical modelling, and is a matter of great relevance in multiple fields such as aviation, meteorology or astrophysics.

The first major task of this Graduation Thesis is to construct a code from scratch that solves the 1D equations of fluid dynamics. The code is written in *Python*. It will solve numerically the whole system of equations in the one-dimensional case (2.7-2.9). Introducing the expression of the internal energy for an ideal gas $\rho\epsilon = \frac{p}{\gamma-1}$ the volumetric densities for mass, momentum and total energy can be reduced to:

$$u_m = \rho \qquad u_c = \rho v \qquad u_e = \frac{p}{\gamma-1} + \rho\frac{v^2}{2} . \tag{2.19}$$

On the other hand, the mass, momentum and energy fluxes can be rewritten as:

$$f_m = \rho\, v = u_c , \tag{2.20}$$

$$f_c = \rho\, v^2 + p = \frac{u_c^2}{u_m} + (\gamma-1)u_e - \frac{u_c^2}{2\,u_m} , \tag{2.21}$$

$$f_e = \left(\rho\frac{v^2}{2} + \frac{\gamma}{\gamma-1}p\right)v = \gamma\, u_e\, v + (1-\gamma)\frac{u_c^3}{2\,u_m^2} . \tag{2.22}$$

Then, the fundamental fluid dynamics equations can be written as conservation equations:

$$\frac{\partial \mathbf{u}}{\partial t} = -\frac{\partial \mathbf{f}(\mathbf{u})}{\partial x} , \tag{2.23}$$

with $\mathbf{u} = (u_m,\, u_c,\, u_e)$ and $\mathbf{f}(\mathbf{u}) = (f_m,\, f_c,\, f_e)$.

In order to solve the differential equations and compute the evolution of the state of the fluid in a discretized manner, a finite difference method is used. The spatial domain is split into a numerical grid of `nint` cells between the ends of the spatial domain x_0 and x_f, separated by a fixed step Δx. The time domain will be split in subsequent t_n times, separated by a variable Δt step that depends on the maximum information propagation speed as commented below. The finite difference methods use a *numerical scheme* to update the densities $\mathbf{u}$ after each time-step. A numerical scheme is an algorithmic process used to update the solution from any given timestep at time t_n to the next one, at time $t_n + \Delta t$. We have introduced two different schemes in the code, the *Lax-Friedrichs scheme* and a scheme of the *Lax-Wendroff* family. They are explained and compared in the next sections.

2.2.1 Lax-Friedrichs scheme

The first scheme we have introduced in the code is the so-called *Lax-Friedrichs scheme* [Toro 2009]. This is a robust and easy to implement explicit finite difference method. It is a FTCS (*Forward in Time, Centered in Space*) scheme. One substitutes the derivatives in space through the simplest centered finite differences, and for the derivatives in time, one uses a simple forward finite difference, while the time advance uses neighboring grid point averages. The update in time is calculated by:

$$\mathbf{u}_i^{n+1} = \frac{\mathbf{u}_{i-1}^n + \mathbf{u}_{i+1}^n}{2} - \frac{\Delta t}{2\,\Delta x}\left[\mathbf{f}\left(\mathbf{u}_{i+1}^n\right) - \mathbf{f}\left(\mathbf{u}_{i-1}^n\right)\right] \ , \tag{2.24}$$

where the subscript i indicates spatial position and the superscript n indicates time: $\mathbf{u}_i^n = \mathbf{u}(x_i,\, t_n)$. Given that the values of the variables at the end of the spatial domain cannot be calculated through the scheme, an extra guard cell is added to each side. Having a total of `nint`+2 cells the extra points will be calculated with the periodic boundary conditions:

$$\mathbf{u}_0^{n+1} = \mathbf{u}_{-2}^n \qquad\qquad \mathbf{u}_{-1}^{n+1} = \mathbf{u}_1^n \ . \tag{2.25}$$

With a fixed spatial resolution of Δx, the time step Δt has to be limited to fulfill the Courant-Friedrichs-Lewy criterion (Courant et al. 1967, Laney 1998, Toro 2009). This condition imposes a maximum timestep for the numerical advance of the calculation which is inversely proportional to the speed of signal propagation in the physical system. In fact, the condition stipulates that $\Delta t < f_{CFL} \cdot \Delta x / v_{sign}$, with v_{sign} the signal propagation speed and f_{CFL} a number of order unity. For an explicit numerical scheme like the one used, the f_{CFL} factor has to be smaller than 1.

2.2.2 Lax-Wendroff scheme

The *Lax-Friedrichs* scheme is simple and robust, but it is also too dissipative. After a number of iterations the amplitude of the perturbation is reduced, as if there were a real energy dissipation effect. In order to solve this problem, a first-generation numerical scheme has been implemented, which belongs to the so-called *Lax-Wendroff* family of schemes, namely the MacCormack scheme. This scheme is implemented in two successive steps; the first one is a FTBS (*Forward in Time, Backward in Space*) finite difference step, while the other is a FTFS (*Forward in Time, Forward in Space*) step. Alternating the order of these steps every iteration achieves good stability properties and second order accuracy in space and time. From the initial densities $\mathbf{u_i^n}$, the corresponding fluxes are calculated $\mathbf{f}(\mathbf{u_i^n})$. Then intermediate density values are calculated. With the FTBS scheme first:

$$\overline{\mathbf{u}}_\mathbf{i}^\mathbf{n} = \mathbf{u_i^n} - \frac{\Delta t}{\Delta x}[\mathbf{f}(\mathbf{u_i^n}) - \mathbf{f}(\mathbf{u_{i-1}^n})] \ . \tag{2.26}$$

Then the FTFS scheme is used:

$$\overline{\overline{\mathbf{u}}}_\mathbf{i}^\mathbf{n} = \overline{\mathbf{u}}_\mathbf{i}^\mathbf{n} - \frac{\Delta t}{\Delta x}[\mathbf{f}(\overline{\mathbf{u}}_\mathbf{i+1}^\mathbf{n}) - \mathbf{f}(\overline{\mathbf{u}}_\mathbf{i}^\mathbf{n})] \ . \tag{2.27}$$

And the final density value is an average of the initial and this last value calculated:

$$\mathbf{u_i^{n+1}} = \frac{\mathbf{u_i^n} + \overline{\overline{\mathbf{u}}}_\mathbf{i}^\mathbf{n}}{2} \ . \tag{2.28}$$

The next iterations will be essentially the same but changing the FTBS-FTFS order.

2.3 Results

To ensure the capabilities of the code to properly solve fluid dynamics problems, we have thoroughly tested it. Firstly the simple analytical propagation of linear sound waves is compared with the numerical results of small perturbation propagation. Then the more demanding case of shock waves, including strong shocks, is studied.

2.3.1 Sound wave tests

The small-amplitude sound wave properties were discussed in Section 2.1.2. According to what was explained there, if an equilibrium state is created with a small-amplitude perturbation added as the initial condition, the whole perturbation should propagate with the same shape and phase speed, $c_{seq} = \sqrt{\gamma \frac{p_{eq}}{\rho_{eq}}}$. If one jumps to a reference frame moving with this speed, equivalent to making $v_{eq} = -c_{seq}$, the perturbation should stay unchanged. This change of reference system can be done because sound waves propagate at c_{seq} with respect to the fluid

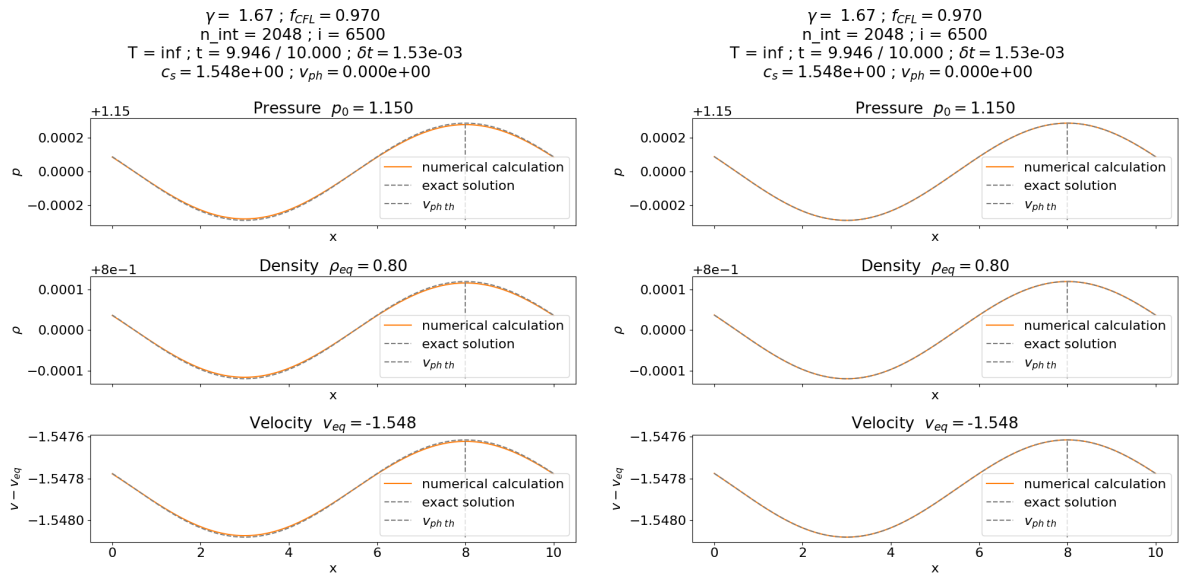

(a) *Lax-Friedrichs* scheme.

(b) *Lax-Wendroff* scheme.

Figure 1: Basic test of the code comparing two different numeric schemes. The initial perturbation is a small amplitude cosine wave. The analytical solution is displayed as the grey dashed line. It corresponds to the shift of the original perturbation with speed $v_{eq} + c_{seq}$. As the initial speed was $v_{eq} = -c_{seq}$, the analytical solution stays still. A video animation of Figure 1a can be seen here.

nints		**2048**	**4096**	**8192**	**16384**
Lax-Friedrichs	displacement	0.0049	0.0049	0.0037	0.0031
	grid points displaced	1	2	3	5
Lax-Wendroff	displacement	0.0049	0.0049	0.0037	0.0031
	grid points displaced	1	2	3	5

Table 1: Numerical solution displacement from the exact solution for sound waves of Figure 1.

at rest, so if in another reference system the fluid has equilibrium speed v_{eq}, the propagation speed is $v_{ph} = c_{seq} + v_{eq}$.

This is the first test carried out in Figure 1. The same experiment was developed using the *Lax-Friedrichs* scheme in Figure 1a and the *Lax-Wendroff* scheme in Figure 1b. We defined an equilibrium state: $p_{eq} = 1.15$, $\rho_{eq} = 0.8$, $v_{eq} = -\sqrt{\gamma \frac{p_{eq}}{\rho eq}}$, as shown in each subplot header. Then, we added to the equilibrium state an initial perturbation with the shape of a cosine with wavelength $\lambda = 10$. If it propagated with phase speed c_{seq}, after a time $t \sim 10$, equivalent to 1.5 wave periods, the perturbation would have travelled 15 distance units. Instead, given the frame of reference used in the calculations, the numerical solution does not practically move compared with the analytical one, marked by the dashed static perturbation in the plot. The displacement is given in Table 1, generated by repeating the exact same experiment and increasing the number

nints	**2048**	**4096**	**8192**	**16384**
Lax-Friedrichs	8.66e-03	4.33e-03	2.16e-03	1.07e-03
Lax-Wendroff	1.7e-05	1.7e-05	1.7e-05	1.7e-05

Table 2: Relative error due to dissipation for both numeric schemes of Figure 1 at $t = 10$ and improving the spatial resolution.

of grid points `nints` used each time. There is an added row that indicates how many grid points correspond to each displacement, illustrating that many distances are equal because of the quantization of space in a numerical grid. The total displaced distance decreases when the spatial resolution is increased in the calculations, proving that the error is due to numerical precision.

Both numeric schemes obtain the same phase speed for perturbations, (same displacement), but the *Lax-Friedrichs* scheme is much more dissipative than the *Lax-Wendroff* scheme, as can be seen in Table 2. It displays the relative error in the calculations of the maximum of the perturbation compared to the exact perturbation. The *Lax-Friedrichs* scheme is two orders of magnitude more dissipative than the *Lax-Wendroff*, and like we expected, increases its accuracy as the spatial resolution is improved.

2.3.2 Tests for shock waves

The elementary theory of shock waves, as discussed in Section 2.1.3, provides the value of the pressure and density jumps and of the postshock Mach number as a function of the incoming Mach number M_0 through equations (2.16-2.18). Setting the initial preshock values ρ_0, p_0, v_0, and specifying the desired M_0, all postshock values are determined by the previous relationships. For the tests in this section, an initial condition is specified basically as a step function, but, in fact, with a hyperbolic tangent profile, to prevent the appearance of singularities in the numerical calculation. Then, the numerical solution should evolve as the expected shock. If $v_0 = 0$, the preshock medium will be at rest and the shock front will advance towards it with speed $V_{sh} = v_0 - u_0 = -u_0 = M_0\, c_{s0}$. Yet, to simplify the analysis of the results, we will jump onto a reference frame in which the shock front is static by establishing $v_0 = u_0 = -M_0\, c_{s0} = -M_0\sqrt{\gamma p_0/\rho_0}$.

Figure 2 shows the results of this simple shock test for a case with $M_0 = 2$, which is intermediate between the limits of weak and strong shock. The same experiment was carried out using the *Lax-Friedrichs* scheme (Figure 2a), the *Lax-Wendroff* scheme (Figure 2b) and the *Lax-Wendroff* scheme with artificial viscosity (Figure 2c), which will be explained in the next paragraph.

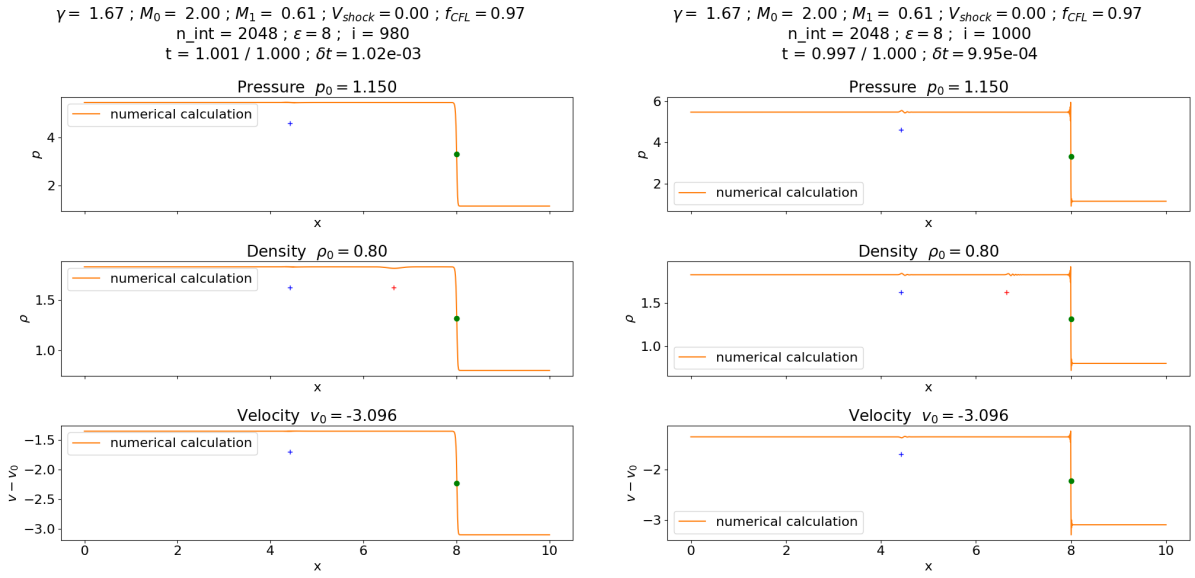

(a) *Lax-Friedrichs* scheme

(b) *Lax-Wendroff* scheme

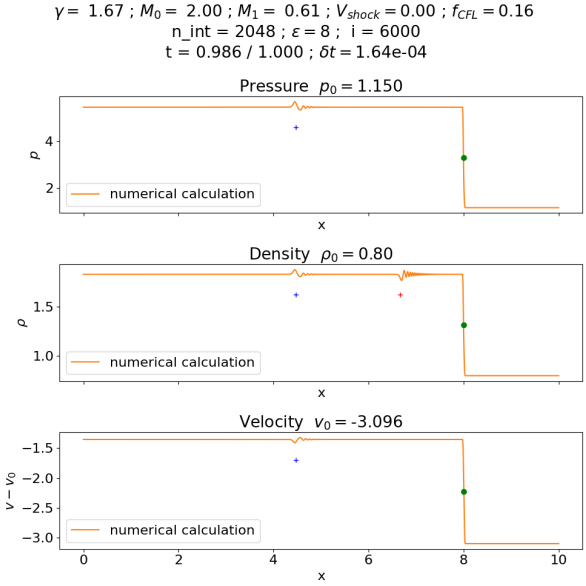

(c) *Lax-Wendroff* scheme using artificial viscosity

Figure 2: $M_0 = 2$ shock test. The obtained jumps correspond to the analytical expressions (2.16-2.18).

In all plots there is a green dot that moves with the theoretical value of V_{sh}. In this case, as $V_{sh} = 0$, the dot is static. The shock front stays basically fixed onto the dot, as shown in Table 3. It displays the distance between the shock front and its theoretical position for different grid point numbers. As separation decreases when spatial resolution increases, the displacement can be considered due to numerical precision. This proves that the numerical calculation of the shock speed is consistent with the expected results.

nints		**2048**	**4096**	**8192**	**16384**
Lax-Friedrichs	displacement	0.0191	0.0098	0.0049	0.0024
	grid points displaced	4	4	4	4
Lax-Wendroff	displacement	0.0191	0.0098	0.0061	0.0024
	grid points displaced	4	4	5	4
L-W artificial viscosity	displacement	0.0191	0.0098	0.0049	0.0024
	grid points displaced	4	4	4	4

Table 3: Numerical solution displacement from exact position for shock waves of Figure 2.

In all three cases two additional small perturbations are apparent in the postshock region (more visible in Figure 2c). The first one, marked with a blue cross, is present in the pressure, density and velocity profiles. The perturbation is in phase for pressure and density, and antiphase for velocity, because it consists of a sound wave that propagates through the postshock medium to the left, travelling with speed $-(|u_1|+c_{s1})$. The perturbation is caused by the small but unavoidable difference between the imposed initial condition and the real shape that the shock takes. The second perturbation, marked with a red cross, is only present in the density profile because it corresponds to a contact discontinuity. Like all contact discontinuities, it moves in step with the medium in which it is located, in this case, the postshock medium, so it travels with speed u_1 to the left.

The calculation of derivatives across the shock is particularly difficult for the numerical scheme due to the abrupt transitions. As a result a series of ripples appear before and after the shock front (clearly seen in Figure 2b). In order to reduce them, the *Ritchmeyer-Von-Neumann artificial viscosity* [Laney 1998] is included. This method adds an extra component to the momentum and energy fluxes that acts like a viscosity wherever the fluid is being compressed ($\partial v/\partial x < 0$). The extra terms are:

$$f_{c\ art\ visc} = \left(\frac{\epsilon \Delta z}{2}\right)^2 \rho \left(\frac{\partial v}{\partial x}\right)^2 , \tag{2.29}$$

$$f_{e\ art\ visc} = \left(\frac{\epsilon \Delta z}{2}\right)^2 \rho\, v \left(\frac{\partial v}{\partial x}\right)^2 , \tag{2.30}$$

where ϵ is a free parameter. Following the theory for this artificial term [Laney 1998], the free parameter ϵ roughly corresponds to the number of grid points that cover the shock transition and an extra condition is added to the f_{CFL} parameter: $f_{CFL} < 10/\epsilon^2$. This will lead to a smaller time-step, requiring more iterations, as seen in Figure 2 (Δt goes from 10^{-3} to $1.6 \cdot 10^{-4}$, requiring about 6 times more iterations).

Including artificial viscosity eliminates the ripples of the shock front, obtaining a sharp transition, and it has low dissipation thanks to the use of the *Lax-Wendroff* scheme. Nevertheless, the decrease of the time-step will increase the computational effort of the experiments. Now the code can be subjected to strong shock conditions.

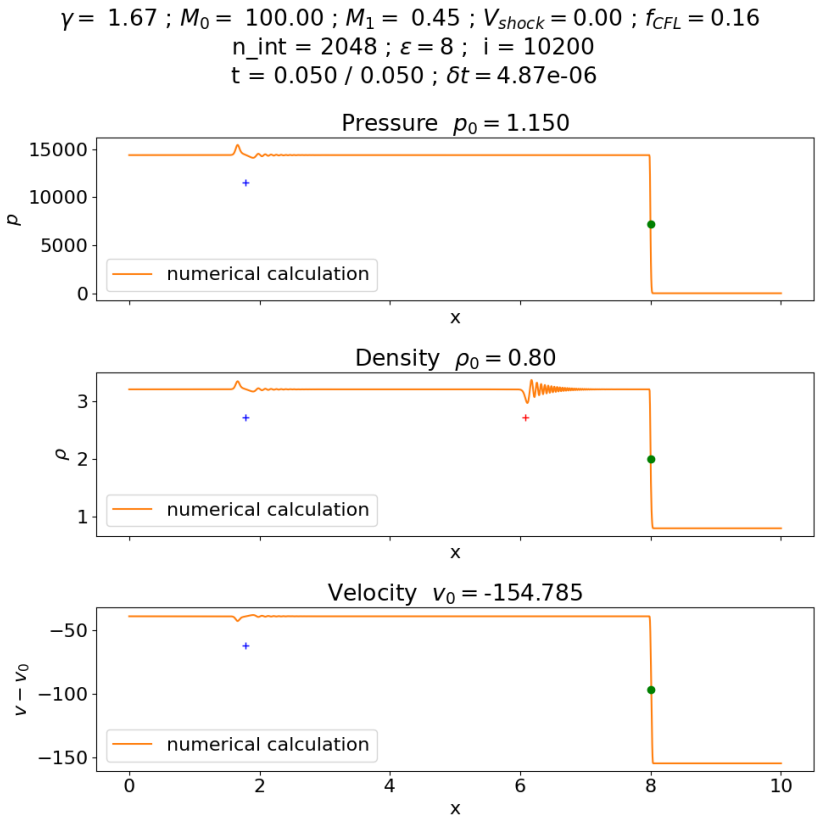

Figure 3: Strong shock test with $M_0 = 100$, using the *Lax-Wendroff* scheme and artificial viscosity. A video animation of this figure can be seen here.

In Figure 3 a strong shock with $M_0 = 100$ is tested. It is verified that the pressure jump is unbounded (4 orders of magnitude difference in the jump) while the density jump is bounded, as expected from equations (2.16-2.18). Even though the jumps are huge, the code yields an accurate solution. The displacement of the shock front to its exact expected position obtained for this case is equivalent to that of Table 3.

3 The standard MHD fluid

En esta sección se derivan las ecuaciones que describen la dinámica de un fluido en presencia de campo electromagnético para el caso unidimensional en el que la velocidad del mismo es paralela a la de propagación y el campo magnético es perpendicular. Se toman las simplificaciones de neutralidad de carga, conductividad infinita y velocidades no relativistas. A continuación se desarrolla la teoría correspondiente a ondas magnetosónicas y choques, y se llevan a cabo una serie de tests para comparar los resultados numéricos con las soluciones analíticas.

After having proved that the code correctly solves the simple non-relativistic ideal fluid equations, we continue by including the electromagnetic field. The fluid is assumed to have an electric charge density per unit volume ρ^{el}, and to support electric currents with electric current vector $\mathbf{j}$. The changes carried out to incorporate to the fluid equations the interaction with the electromagnetic field consist of adding two terms:

- The force exerted by the electromagnetic field on the fluid, i.e., the Lorentz force, given by: $\mathbf{F}_L = \rho^{el}\,\mathbf{E} + \mathbf{j} \times \mathbf{B}$. This is a term that is added to the right of the momentum equation (2.2).
- The work done by the electromagnetic field on the fluid, given by $\mathbf{E} \cdot \mathbf{j}$. This term must be added to the right of the energy equation (2.3).

In the following we will use Maxwell's equations to transform the resulting expressions for the enlarged fluid equations into their explicit conservation form, with the objective of better understanding the nature of the coupled system fluid-electromagnetic field in the non-relativistic approximation. This is usually referred to as the magnetohydrodynamic approximation.

3.1 Equations

To carry out the transformation just mentioned, Poynting's theorem will be used, i.e.:

$$\mathbf{E} \cdot \mathbf{j} = -\mathbf{div}\ \mathbf{S}_p - \frac{\partial u_{em}}{\partial t}\ , \tag{3.1}$$

where $u_{em} = \epsilon_0 \frac{E^2}{2} + \frac{B^2}{2\mu_0}$ is the electromagnetic energy density per unit volume and $\mathbf{S}_p = \frac{\mathbf{E}\times\mathbf{B}}{\mu_0}$ is Poynting's vector. This expression of the work done by the electromagnetic field on the fluid as the sum of a divergence term and a time derivative is convenient for writing the equations in explicit conservation form. The equation itself, i.e., Poynting's theorem, has a clear interpretation in terms of energy conservation: the energy lost by the electromagnetic field in

exerting power onto the fluid comes at the expense of the electromagnetic energy (time derivative term) or through deposition of the electromagnetic energy flux (divergence term).
In order to transform the resulting expressions, Maxwell's equations will be used:

$$\begin{cases} \nabla \cdot \mathbf{E} = \dfrac{\rho^{el}}{\epsilon_0} \ , & (3.2) \\ \nabla \cdot \mathbf{B} = 0 \ , & (3.3) \\ \nabla \times \mathbf{E} = -\dfrac{\partial \mathbf{B}}{\partial t} \ , & (3.4) \\ \nabla \times \mathbf{B} = \mu_0 \left(\mathbf{j} + \epsilon_0 \dfrac{\partial \mathbf{E}}{\partial t} \right) \ , & (3.5) \end{cases}$$

where ϵ_0 and μ_0 denote the permittivity and permeability of free space, respectively.

Using the foregoing equations, and after some amount of straightforward, but non-trivial, algebra, one can transform the expression for the Lorentz force into the sum of a divergence term and a time derivative, as follows:

$$\mathbf{F}_L = \mathbf{div}\ \hat{\mathbf{M}} - \frac{1}{c^2} \frac{\partial \mathbf{S}_p}{\partial t} \ , \tag{3.6}$$

where $\hat{\mathbf{M}} = -\frac{B^2}{2\mu_0}\hat{\mathbf{I}} - \frac{\epsilon_0 E^2}{2}\hat{\mathbf{I}} + \frac{\mathbf{B}\otimes\mathbf{B}}{\mu_0} + \epsilon_0 \mathbf{E} \otimes \mathbf{E}$ is Maxwell's stress tensor.

A further equation is necessary to obtain a complete system, namely Ohm's Law, which links the electric current with the electric and magnetic fields. We borrow its expression from the basic theory of MHD by Priest 2014:

$$\mathbf{j} = \sigma \left(\mathbf{E} + \mathbf{v} \times \mathbf{B} \right) \ , \tag{3.7}$$

where σ denotes electrical conductivity.

3.1.1 The MHD equations

Using the formulae from electromagnetic theory just written and through straightforward derivations, one can turn the equations for the conducting fluid in the presence of an electromagnetic field into the following form, which is in explicit conservation form:

$$\begin{cases} \dfrac{\partial \rho}{\partial t} = -\mathbf{div}(\rho\, \mathbf{v}) \ , & (3.8) \\ \dfrac{\partial \mathbf{B}}{\partial t} = -\mathbf{curl}\, \mathbf{E} \ , & (3.9) \\ \dfrac{\partial}{\partial t} \left(\rho\, \mathbf{v} + \dfrac{\mathbf{S}_p}{c^2} \right) = -\mathbf{div} \left(\rho\, \mathbf{v} \otimes \mathbf{v} + p\, \hat{\mathbf{I}} - \hat{\mathbf{M}} \right) \ , & (3.10) \\ \dfrac{\partial}{\partial t} \left(\rho\, \epsilon + \rho \dfrac{v^2}{2} + u_{em} \right) = -\mathbf{div} \left[\left(\rho\, \epsilon + \rho \dfrac{v^2}{2} + p \right) \mathbf{v} + \mathbf{S}_p \right] \ . & (3.11) \end{cases}$$

Equations (3.10) and (3.11) contain now the conservation of momentum and energy of the combined fluid and electromagnetic field system. The term $\mathbf{S}_p/c^2$ clearly represents the momentum

density of the electromagnetic field per unit volume, the tensor $\hat{\mathbf{M}}$ is a stress tensor due to the electromagnetic field, the u_{em} term is the energy density of the electromagnetic field per unit volume and the $\mathbf{S}_p$ vector is the energy flux vector associated with the electromagnetic field.

Now, a number of further simplifications are assumed in the basic MHD theory:

- CHARGE NEUTRALITY. This means that $\rho^{el} \to 0$, leaving the Lorentz force as $\mathbf{F}_L = \mathbf{j} \times \mathbf{B}$ and (3.2) as $\nabla \cdot \mathbf{E} = 0$.

- INFINITE CONDUCTIVITY, while keeping finite currents. Applying it to Ohm's Law, if $\sigma \to \infty$ and $\mathbf{j}$ is finite, the electric field is $\mathbf{E} = -\mathbf{v} \times \mathbf{B}$.
  Then the Poynting vector can be rewritten as $\mathbf{S}_p = \frac{-(\mathbf{v}\times\mathbf{B})\times\mathbf{B}}{\mu_0}$ and Faraday's induction equation (3.4) is rewritten as $\frac{\partial \mathbf{B}}{\partial t} = \nabla \times (\mathbf{v} \times \mathbf{B})$.

- NON-RELATIVISTIC FLUID SPEEDS: $v \ll c$, where c is the speed of light. Considering this:

  – The electromagnetic energy density is dominated by the magnetic energy density:

  $$\frac{\epsilon_0 E^2}{B^2/\mu_0} = \epsilon_0 \mu_0 \frac{|\mathbf{v} \times \mathbf{B}|^2}{B^2} \leq \frac{v^2}{c^2} \ll 1 \ , \tag{3.12}$$

  as $c = 1/\sqrt{\epsilon_0 \mu_0}$.

  – The Ampère-Maxwell law (3.5) is also dominated by the magnetic term:

  $$\frac{\mu_0 \epsilon_0 \partial \mathbf{E}/\partial t}{\nabla \times \mathbf{B}} = \frac{1}{c^2} \frac{|\mathbf{v} \times \mathbf{B}| \tau^{-1}}{|\mathbf{B}| L^{-1}} \leq \frac{|\mathbf{v}| L/\tau}{c^2} \ll 1 \ , \tag{3.13}$$

  where L and τ represent the characteristic variation distance of $\mathbf{B}$ and characteristic variation time of $\mathbf{E}$. When the speed of all waves propagating in the system are non-relativistic, $L/\tau \ll c$. Then, the Ampère-Maxwell law (3.5) can be rewritten as:

  $$\nabla \times \mathbf{B} = \mu_0 \mathbf{j} \ , \tag{3.14}$$

  i.e., the displacement current term can be neglected.

  – Following the previous reasoning, the magnetic field terms dominate over the electric field terms in Maxwell's stress tensor, so it can be rewritten as $\hat{\mathbf{M}} = -\frac{B^2}{2\mu_0}\hat{\mathbf{I}} + \frac{\mathbf{B}\otimes\mathbf{B}}{\mu_0}$.

  – The electromagnetic momentum density is given by $\mathbf{S}_p/c^2$, and comparing it with the fluid momentum density

  $$\frac{|\mathbf{S}_p/c^2|}{|\rho \mathbf{v}|} = \frac{|(\mathbf{v} \times \mathbf{B}) \times \mathbf{B}|}{\mu_0 c^2 \rho |\mathbf{v}|} \leq \frac{B^2}{\mu_0 \rho} \frac{1}{c^2} = \frac{v_A^2}{c^2} \ll 1 \ . \tag{3.15}$$

Applying these simplifications, the resulting system of equations is:

$$\begin{cases} \dfrac{\partial \rho}{\partial t} = -\mathbf{div}(\rho\,\mathbf{v}) \ , & (3.16) \\ \dfrac{\partial \mathbf{B}}{\partial t} = \mathbf{curl}(\mathbf{v}\times\mathbf{B}) \ , & (3.17) \\ \dfrac{\partial}{\partial t}(\rho\,\mathbf{v}) = -\mathbf{div}\left[\rho\,\mathbf{v}\otimes\mathbf{v} + p\,\hat{\mathbf{I}} + \dfrac{B^2}{2\mu_0}\hat{\mathbf{I}} - \dfrac{\mathbf{B}\otimes\mathbf{B}}{\mu_0}\right] \ , & (3.18) \\ \dfrac{\partial}{\partial t}\left(\rho\,\epsilon + \rho\dfrac{v^2}{2} + \dfrac{B^2}{2\mu_0}\right) = -\mathbf{div}\left[\left(\rho\,\epsilon + \rho\dfrac{v^2}{2} + p\right)\mathbf{v} - \dfrac{(\mathbf{v}\times\mathbf{B})\times\mathbf{B}}{\mu_0}\right] \ . & (3.19) \end{cases}$$

The term $\frac{B^2}{2\mu_0}$ is called magnetic pressure, so the total pressure will be the sum of the gas and magnetic pressures: $p_{tot} = p_{gas} + p_{mag} = p + \frac{B^2}{2\mu_0}$.

Similarly to what we did for standard simple fluids, we will be here considering a one-dimensional system. For extra simplification, we will limit ourselves to the case when the magnetic field $\mathbf{B}$ is perpendicular to $\mathbf{v}$, i.e.: $\rho = \rho(x),\ p = p(x),\ \mathbf{v} = v(x)\mathbf{e_x},\ \mathbf{B} = B(x)\mathbf{e_z}$. The system of equations can then be written as:

$$\begin{cases} \dfrac{\partial \rho}{\partial t} = -\dfrac{\partial}{\partial x}(\rho\,v) \ , & (3.20) \\ \dfrac{\partial B}{\partial t} = -\dfrac{\partial}{\partial x}(B\,v) \ , & (3.21) \\ \dfrac{\partial}{\partial t}(\rho\,v) = -\dfrac{\partial}{\partial x}\left[\rho\,v^2 + p + \dfrac{B^2}{2\mu_0}\right] \ , & (3.22) \\ \dfrac{\partial}{\partial t}\left(\rho\,\epsilon + \rho\dfrac{v^2}{2} + \dfrac{B^2}{2\mu_0}\right) = -\dfrac{\partial}{\partial x}\left[\left(\rho\,\epsilon + \rho\dfrac{v^2}{2} + p + \dfrac{B^2}{\mu_0}\right)v\right] \ . & (3.23) \end{cases}$$

The one-dimensional version of the induction equation (3.21) adds an important insight to the situation. The magnetic flux contained between two fluid elements will be constant in time:

$$\begin{aligned} \Phi(t) &= \int_{x_0(t)}^{x_1(t)} B(x,t)dx \ ; \\ \frac{d\Phi(t)}{dt} &= \int_{x_0(t)}^{x_1(t)} \frac{\partial B(x,t)}{\partial t}dx + B(x_1,t)\frac{dx_1(t)}{dt} - B(x_0,t)\frac{dx_0(t)}{dt} = 0 \ . \end{aligned}$$

This result is a consequence in our 1D system of the general result for the 3D case called 'the flux freezing theorem', studied in standard MHD texts.

3.1.2 Magnetosonic waves

Following the steps of Section 2.1.2, the small-perturbation theory for our 1D MHD system with transverse magnetic field (3.20-3.23) can be briefly sketched. Expanding the equations as

a power series in the perturbations and disregarding all non-linear terms we obtain:

$$\begin{cases} \dfrac{\partial}{\partial t}\left(\dfrac{\rho'}{\rho_{eq}}\right) = -v_{ph}\ \dfrac{\partial}{\partial x}\left(\dfrac{v'}{v_{ph}}\right)\ , & (3.24)\\ \dfrac{\partial}{\partial t}\left(\dfrac{B'}{B_{eq}}\right) = -v_{ph}\ \dfrac{\partial}{\partial x}\left(\dfrac{v'}{v_{ph}}\right)\ , & (3.25)\\ \dfrac{\partial}{\partial t}\left(\dfrac{v'}{v_{ph}}\right) = -\dfrac{1}{v_{ph}}\left[\dfrac{c_{s_{eq}}^2}{\gamma}\ \dfrac{\partial}{\partial x}\left(\dfrac{p'}{p_{eq}}\right) + v_{A_{eq}}^2\ \dfrac{\partial}{\partial x}\left(\dfrac{B'}{B_{eq}}\right)\right]\ , & (3.26)\\ \dfrac{\partial}{\partial t}\left(\dfrac{p'}{p_{eq}}\right) = -\gamma\, v_{ph}\ \dfrac{\partial}{\partial x}\left(\dfrac{v'}{v_{ph}}\right)\ , & (3.27) \end{cases}$$

where v_{ph} is the quantity that compares to v' in establishing the amplitude of the perturbation, and will denote the phase speed, and $v_A = B/\sqrt{\mu_0 \rho}$ is the Alfvén speed. Following the same steps as before, it can be determined that the phase speed is $v_{ph} = \sqrt{c_{s_{eq}}^2 + v_{A_{eq}}^2} = c_{ms}$, a quantity known as magnetosonic speed. Like for the elementary sound waves, the phase speed is independent of k, so magnetosonic waves are also non-dispersive. The amplitude relations of the perturbations are: $\frac{\rho'}{\rho_{eq}} = \frac{B'}{B_{eq}} = \frac{1}{\gamma}\frac{p'}{p_{eq}} = \pm\frac{v'}{(c_{ms})_{eq}}$. The density, magnetic field and gas pressure perturbations are in phase, while the velocity perturbation can be in phase or antiphase, depending on the direction of propagation.

3.1.3 Shocks

Non-relativistic MHD shocks are studied in the same situation as classical ideal fluid shocks in Section 2.1.3. Jump relations across them are obtained in all the classical books about magnetohydrodynamics, like those of Boyd et al. 2003 or Priest 2014, and are shown below. The plasma beta for the unshocked region is defined as:

$$\beta_0 = \frac{p_{gas0}}{p_{mag0}} = \frac{2\,\mu_0\, p_0}{B_0^2} = \frac{2\, c_{s0}^2}{\gamma\, v_{A0}^2} \tag{3.28}$$

Remembering the sonic Mach number of the shock $M_0 = \frac{|u_0|}{c_{s0}}$, the jump relations are given by:

$$\begin{cases} \dfrac{\rho_1}{\rho_0} = X\ , & (3.29)\\ \dfrac{B_1}{B_0} = X\ , & (3.30)\\ \dfrac{u_1}{u_0} = X^{-1}\ , & (3.31)\\ \dfrac{p_1}{p_0} = 1 + \gamma\, M_0^2(1 - X^{-1}) + \beta_0^{-1}(1 - X^2)\ , & (3.32) \end{cases}$$

where X is the positive solution of:

$$f(X) = 2(2-\gamma)X^2 + \Big[2\beta_0 + (\gamma-1)\beta_0 M_0^2 + 2\Big]\,\gamma X - \gamma(\gamma+1)\beta_0 M_0^2 = 0\ . \tag{3.33}$$

If $M_0 \to \infty$, $X \to \frac{\gamma+1}{\gamma-1}$, so jumps across density, magnetic field and relative velocities to the shock front are bounded, and the bound is the same as for density and relative velocities in the purely hydrodynamic situation (2.17-2.18). Like in that case, the pressure jump is also unbounded for high M_0, because as the incoming energy flux is unbounded, the outgoing energy flux has to be unbounded too.

For high β_0, the gas pressure is more relevant than the magnetic pressure. If $\beta_0 \to \infty$, $X \to \frac{(\gamma+1)M_0^2}{2+(\gamma-1)M_0^2}$, and then $\frac{\rho_0}{\rho_1} = X^{-1}$, i.e., the purely hydrodynamic case (2.17) is recovered.

Both tendencies can be appreciated in Figure 4. For $\gamma = 5/3$, when $M_0 \to \infty$, it is seen in the top left plot that $\rho_1/\rho_0 \to 4$ and in the center left plot $p_1/p_0 \to \infty$. Furthermore, both figures show that when β_0 increases, the behaviour of the curve approximates the hydrodynamic values previously calculated. In addition, when $M_0 \to \infty$, all β_0 curves take the same behaviour (even though they may have different values) because as the incoming energy flux increases, the relevant dynamic term that increases unboundedly the outgoing energy flux is the gas pressure.

3.2 Numerical solution

The one-dimensional MHD system (3.20-3.23) is highly non-linear and an exact analytical solution is very difficult or impossible to find, as for the classical ideal fluid case commented in Section 2.2. It has to be solved through numerical methods, carrying out computational fluid magnetohydrodynamical simulations. The numeric scheme used is the *Lax-Wendroff* scheme with the *Von-Neumann* artificial viscosity included. The difference now is the calculation of numerical densities and fluxes, given by the system of non-linear equations (3.20-3.23). The volumetric densities of mass, momentum and energy and the equivalent numerical quantity for the magnetic field are:

$$u_m = \rho \ , \qquad u_B = B \ , \qquad u_c = \rho\, v \ , \qquad u_e = \frac{p}{\gamma-1} + \rho\frac{v^2}{2} + \frac{B^2}{2\mu_0} \ . \tag{3.34}$$

On the other hand, the mass, momentum and energy fluxes and the equivalent quantity for the magnetic field are left as:

$$f_m = \rho\, v = u_c \ , \tag{3.35}$$

$$f_B = B\, v = u_B \frac{u_c}{u_m} \ , \tag{3.36}$$

$$f_c = \rho\, v^2 + p + \frac{B^2}{2\mu_0} = (\gamma-1)u_e + \left(\frac{3}{2} - \gamma\right)\frac{u_c^2}{u_m} + (2-\gamma)\frac{u_B^2}{2\mu_0} \ , \tag{3.37}$$

$$f_e = \left(\rho\frac{v^2}{2} + \frac{\gamma}{\gamma-1}p + \frac{B^2}{\mu_0}\right) v = \left[\gamma\, u_e + (1-\gamma)\frac{u_c^2}{2u_m} + \left(1 - \frac{\gamma}{2}\right)\frac{u_B^2}{\mu_0}\right]\frac{u_c}{u_m} \ . \tag{3.38}$$

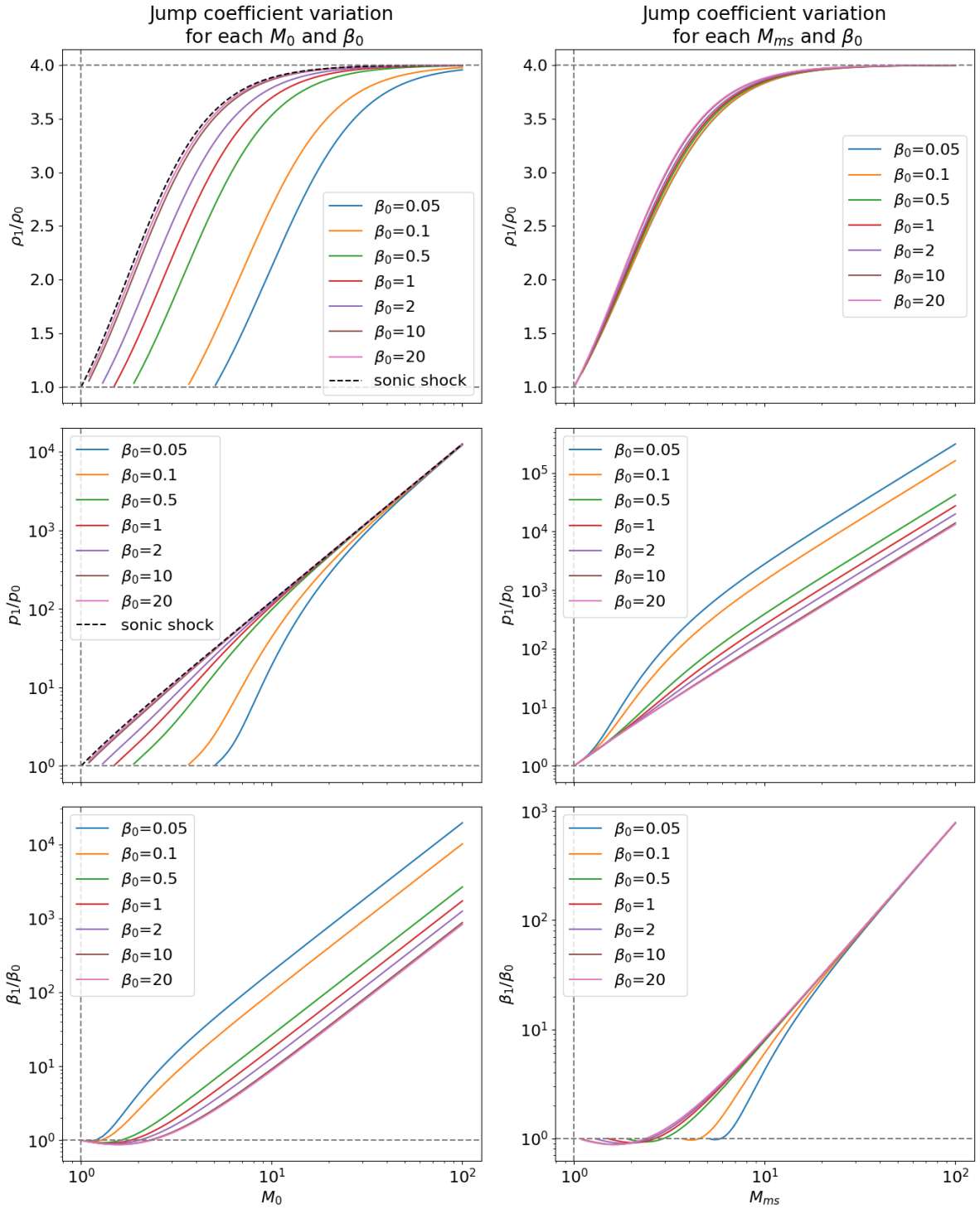

Figure 4: Variation of density, pressure and β jumps with respect to both M_0 and M_{ms0}

nints		2048	4096	8192	16384
$\beta_{eq} = 10$	displacement	0.0049	0.0049	0.0037	0.0031
	grid points displaced	1	2	3	5
$\beta_{eq} = 0.5$	displacement	0.0098	0.0073	0.0061	0.0061
	grid points displaced	2	3	5	10

Table 4: Numerical solution displacement from exact position of Figure 5.

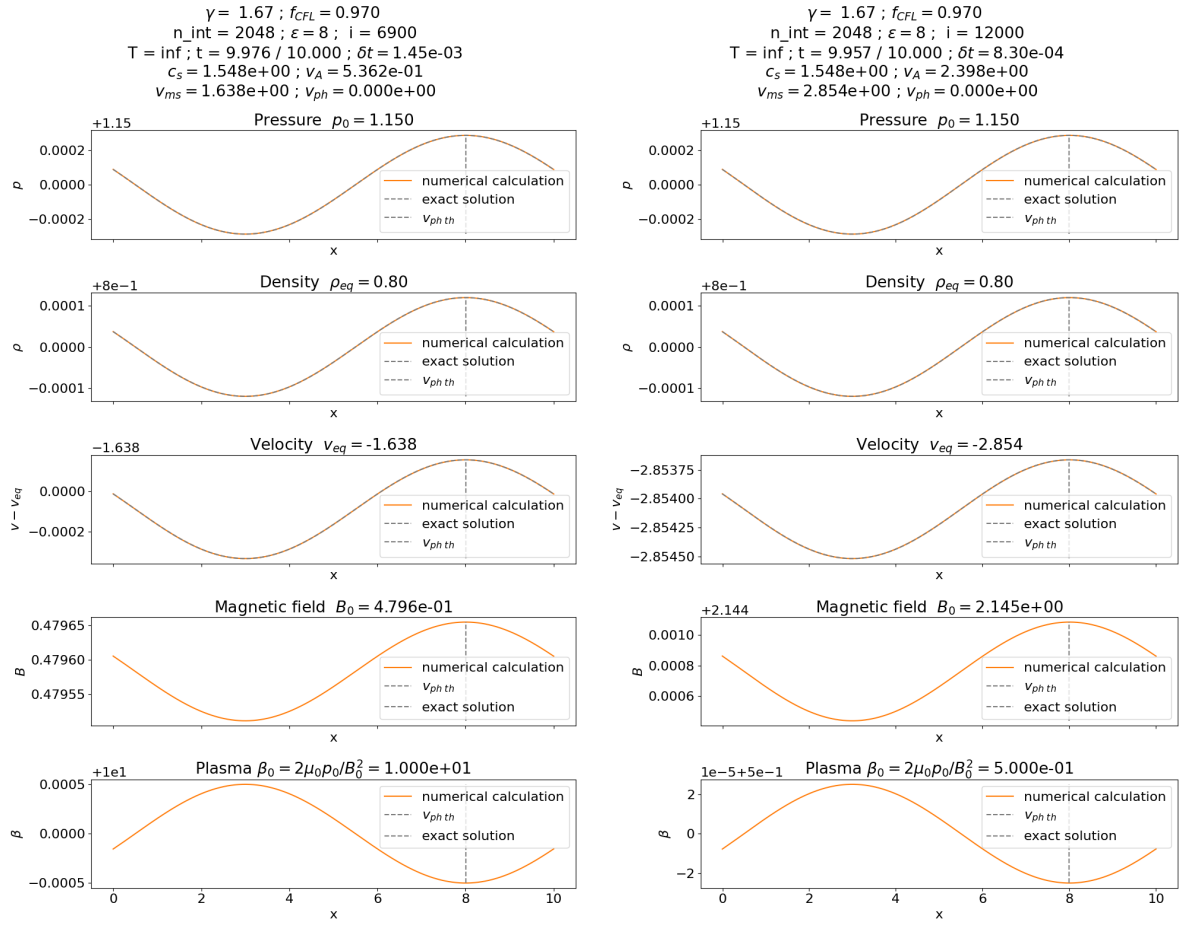

Figure 5: Basic magnetosonic wave test for the MHD case. The gray dashed line is the analytical solution, a static perturbation, which matches the numerical calculation performed by the program. The left hand side corresponds to a $\beta_0 = 10$ situation, and time elapsed is equivalent to 1.6 periods of the perturbation. The right hand side corresponds to a $\beta_0 = 0.5$ situation, and the time elapsed corresponds to 2.8 periods. A video animation of this figure can be seen here.

3.3 Results

3.3.1 Magnetosonic wave test

As explained in Section 2.3.1, if a small amplitude perturbation is added to the equilibrium state as the initial condition, the perturbation will propagate with phase speed $v_{ph} = (c_{ms})_{eq} = \sqrt{c_{s_{eq}}^2 + v_{A_{eq}}^2}$. If the initial velocity of the fluid in the equilibrium state is $v_{eq} = -v_{ph}$, the

perturbation will appear static. The results of the experiment for equilibrium values $p_{eq} = 1.15$, $\rho_{eq} = 0.8$, and two different values for the plasma beta, namely $\beta_{eq} = 10$ and $\beta_{eq} = 0.5$, are shown in Figure 5. For the experiments, we added a small-amplitude perturbation with cosine shape and wavelength $\lambda = 10$. Like in Figure 1, after a time $t \sim 10$, the perturbation has remained almost static. Its displacement from the exact theoretical position, i.e., the error, is measured in Table 4. The error decreases as spatial resolution is increased, confirming the ability of the calculations of the code to match the analytical results.

3.3.2 Shock test

The shock wave theory in section 3.1.3 presented the jump relations for a magnetosonic shock. In the frame of reference that moves with the shock front, the shock should appear static.
We have carried out three experiments for shocks, all with $M_0 = 10$, but with different values of β_0, namely $\beta_0 = 0.1$, 1 and 10; this was achieved by changing B_0. The results are illustrated in Figure 6. Now, instead of displaying the p_{gas} profile, the p_{tot} profile is drawn. As expected, the shock front stays at a fixed position close to the theoretical location marked with the static green dot. The numerical errors lead to a slight displacement of the shock, which is listed in Table 5 for the different cases. This means that the numeric V_{sh} matches the theoretical value expected. In all different β_0 cases secondary perturbations similar to those encountered for simple sonic shocks in Section 2.3.2 are present. The magnetosonic wave that propagates to the left through the postshock medium matches its predicted speed, just like the contact discontinuity. The latter is absent in the total pressure profile, as expected.

Up to this point, the theory of MHD perturbation propagation has been explained and tested with a numerical code. The simplifications assumed of charge neutrality and very large conductivity while keeping finite currents correspond to the treatment of plasmas found throughout the universe. However, the assumption of non-relativistic signal speed propagation is a more restrictive simplification that does not always hold. There are certain cases in which the Alfvén speed, v_A, can reach extremely high values, becoming relativistic. If fluid speeds are still much smaller than the speed of light, a semi-relativistic system can be considered.

nints		**2048**	**4096**	**8192**	**16384**
$\beta_0 = 0.1$	displacement	0.0191	0.0098	0.0049	0.0024
	grid points displaced	4	4	4	4
$\beta_0 = 1$	displacement	0.0191	0.0098	0.0049	0.0024
	grid points displaced	4	4	4	4
$\beta_0 = 10$	displacement	0.0191	0.0098	0.0049	0.0024
	grid points displaced	4	4	4	4

Table 5: Numerical solution displacement from exact position for Figure 6.

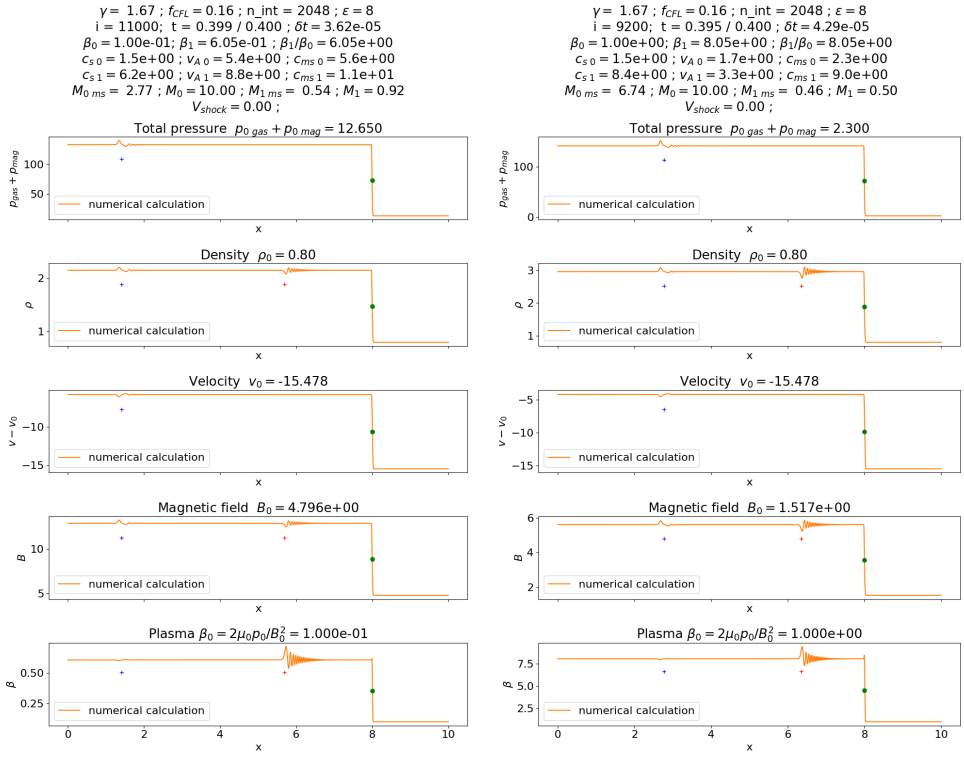

(a) $\beta_0 = 0.1$ (b) $\beta_0 = 1$

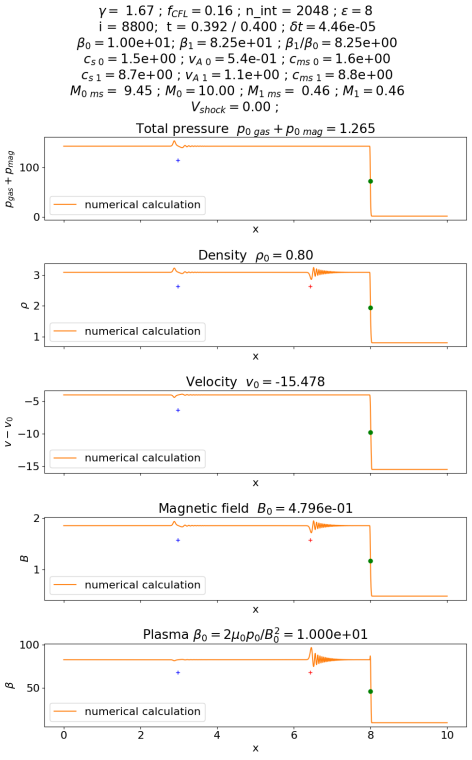

(c) $\beta_0 = 10$

Figure 6: $M_0 = 10$ shock test with different values of β_0. The obtained jumps accurately match the analytical expressions (3.29-3.32). The blue marker moves with speed $|u_1| + c_{ms}$ to the left, the red marker moves with $|u_1|$ speed to the left and the green dot moves with V_{sh} speed, which is zero in this system of reference. A video animation of Figure 6a can be seen here.

4 Semi-relativistic MHD fluid

En la presente sección se derivan las ecuaciones que describen la dinámica de un fluido en presencia de campo electromagnético para el mismo caso unidimensional anterior, a diferencia de que el tratamiento para las ecuaciones del electromagnetismo incluye la corriente de desplazamiento. Se elabora la teoría correspondiente a ondas magnetosónicas en esta situación. Posteriormente se presenta la corrección de Boris, un método que permite reducir el tiempo computacional mediante una elección artificial de velocidad de la luz que limita la velocidad de propagación de señales del sistema. Se llevan a cabo tests de ondas y choques para comprobar los efectos de esta corrección.

In this chapter, we continue considering an ideal fluid (i.e. no dissipative phenomena are included, like heat conduction or viscosity) in interaction with an electromagnetic field, and keep the assumptions of charge neutrality and infinite conductivity. The fluid is still assumed to have non-relativistic speeds, so that the non-relativistic fluid equations can be maintained. The new aspect considered here is the possibility that the signal propagation speed in the plasma, in particular the Alfvén speed, may no longer be very small compared to the speed of light. In this case, the approximation of neglecting the displacement current carried out in Section 3.1.1 (Equations 3.13 and 3.14) cannot be kept. Consequently, the non-relativistic equations of fluid dynamics will be combined with the full system of the Maxwell equations. The theoretical basis for this approach can be found in the papers by Gombosi et al. 2002, Boris 1970, Rempel 2016 and Chen et al. 2022.

In fact, in the solar corona above active regions the Alfvén speed can be very large ($B \approx 300$ G$= 0.03$ T, $\rho \approx 2 \cdot 10^{-12}$ kg/m^3, then $v_A = B/\sqrt{\mu_0 \rho} \approx 2 \cdot 10^4$ km/s), but still well below the speed of light. Yet, in the Boris correction that is tested later in this chapter, the speed of light is reduced artificially, so the Alfvén speed can become close to c, even if only as a trick to speed up the numerical calculation.

4.1 Equations

The starting point will be the general system of equations for MHD fluids (3.8-3.11). The system will be rewritten for the one-dimensional case, and the corresponding simplifications will be applied.

4.1.1 Fully non-linear equations

In the one-dimensional case with purely transverse magnetic field [$\rho = \rho(x)$, $p = p(x)$, $\mathbf{v} = v(x)\,\mathbf{e_x}$, $\mathbf{B} = B(x)\,\mathbf{e_z}$] and under the assumptions of charge neutrality and infinite conductivity, the following simplified equations hold:

$$\mathbf{E} = -\mathbf{v}\times\mathbf{B} = vB\ \mathbf{e_y}\ , \tag{4.1}$$

$$\mathbf{S}_p = \frac{\mathbf{E}\times\mathbf{B}}{\mu_0} = \frac{vB^2}{\mu_0}\mathbf{e_x}\ , \tag{4.2}$$

$$\frac{\partial\mathbf{B}}{\partial t} = -\nabla\times\mathbf{E} = -\frac{\partial(vB)}{\partial x}\mathbf{e_z}\ , \tag{4.3}$$

$$M_{ij} = -\frac{B^2}{2\mu_0}\left(1+\frac{v^2}{c^2}\right)\delta_{ij} + \frac{B^2}{\mu_0}\left(\delta_{iz}\delta_{jz} + \frac{v^2}{c^2}\delta_{iy}\delta_{jy}\right)\ , \tag{4.4}$$

$$u_{em} = \frac{B^2}{2\mu_0} + \frac{\epsilon_0 v^2 B^2}{2} = \frac{B^2}{2\mu_0}\left(1+\frac{v^2}{c^2}\right)\ . \tag{4.5}$$

Then, the whole system (3.8-3.11) can be written for the one-dimensional case as:

$$\begin{cases} \dfrac{\partial\rho}{\partial t} = -\dfrac{\partial}{\partial x}(\rho\, v)\ , & (4.6)\\[2ex] \dfrac{\partial B}{\partial t} = -\dfrac{\partial}{\partial x}(B\, v)\ , & (4.7)\\[2ex] \dfrac{\partial}{\partial t}\left(\rho\, v + \dfrac{vB^2}{\mu_0}\dfrac{1}{c^2}\right) = -\dfrac{\partial}{\partial x}\left[\rho\, v^2 + p + \dfrac{B^2}{2\mu_0}\left(1+\dfrac{v^2}{c^2}\right)\right]\ , & (4.8)\\[2ex] \dfrac{\partial}{\partial t}\left[\rho\,\epsilon + \rho\dfrac{v^2}{2} + \dfrac{B^2}{2\mu_0}\left(1+\dfrac{v^2}{c^2}\right)\right] = -\dfrac{\partial}{\partial x}\left[\left(\rho\,\epsilon + \rho\dfrac{v^2}{2} + p\right)v + \dfrac{vB^2}{\mu_0}\right]\ . & (4.9) \end{cases}$$

The continuity and induction equations remain unchanged, while there are new terms in the momentum and energy conservation equations when compared to the equivalent system (3.20-3.23). The extra terms that appear are marked in blue. These elements can be expressed in terms of the Alfvén velocity, as $\frac{B^2}{\mu_0} = \rho v_A^2$:

$$\frac{\partial}{\partial t}\left(\rho v + \rho v\frac{v_A^2}{c^2}\right) = -\frac{\partial}{\partial x}\left[\rho v^2 + p + \frac{B^2}{2\mu_0} + \rho\frac{v^2}{2}\frac{v_A^2}{c^2}\right]\ , \tag{4.10}$$

$$\frac{\partial}{\partial t}\left(\rho\epsilon + \rho\frac{v^2}{2} + \frac{B^2}{2\mu_0} + \rho\frac{v^2}{2}\frac{v_A^2}{c^2}\right) = -\frac{\partial}{\partial x}\left[\left(\rho\epsilon + \rho\frac{v^2}{2} + p\right)v + \frac{vB^2}{\mu_0}\right]\ . \tag{4.11}$$

As the Alfvén velocity need not be very small compared to c in the present case, the new terms can be relevant in the evolution of the system. We will refer to the ratio $f_B = \frac{v_A}{c}$ as the Boris factor.

It is seen that the effect of the Poynting term in the left hand side of the momentum equation (3.10) has the effect of increasing the inertia of the fluid by a factor f_B. A discussion of this effect and its consequences can be found in the articles by Rempel 2016 and Chen et al. 2022.

4.1.2 Semi-relativistic magnetosonic waves

Following the steps of Sections 2.1.2 and 3.1.2, the theory of magnetosonic waves in the present semi-relativistic context can be derived. For small-amplitude perturbations, considering $v_{eq} = 0$, expanding (4.6-4.9) as a power series in the perturbations and disregarding non-linear terms:

$$\begin{cases} \dfrac{\partial}{\partial t}\left(\dfrac{\rho'}{\rho_{eq}}\right) = -v_{ph}\,\dfrac{\partial}{\partial x}\left(\dfrac{v'}{v_{ph}}\right) , & (4.12) \\ \dfrac{\partial}{\partial t}\left(\dfrac{B'}{B_{eq}}\right) = -v_{ph}\,\dfrac{\partial}{\partial x}\left(\dfrac{v'}{v_{ph}}\right) , & (4.13) \\ \dfrac{\partial}{\partial t}\left(\dfrac{v'}{v_{ph}}\right) = -\dfrac{1}{v_{ph}}\dfrac{c^2}{c^2+v_A^2}\left[\dfrac{c_{s_{eq}}^2}{\gamma}\,\dfrac{\partial}{\partial x}\left(\dfrac{p'}{p_{eq}}\right) + v_{A_{eq}}^2\,\dfrac{\partial}{\partial x}\left(\dfrac{B'}{B_{eq}}\right)\right] , & (4.14) \\ \dfrac{\partial}{\partial t}\left(\dfrac{p'}{p_{eq}}\right) = -\gamma\, v_{ph}\,\dfrac{\partial}{\partial x}\left(\dfrac{v'}{v_{ph}}\right) . & (4.15) \end{cases}$$

Following the steps of previous sections, the phase speed turns out to be:

$$v_{ph} = \sqrt{\frac{c_{s_{eq}}^2 + v_{A_{eq}}^2}{1+\frac{v_{A_{eq}}^2}{c^2}}} = \frac{(c_{ms})_{eq}}{\sqrt{1+f_B^2}} . \tag{4.16}$$

v_{ph} is independent of k, so the semi-relativistic magnetosonic sound waves are non-dispersive. From (4.16) we see that the phase speed of the magnetosonic waves in the present semi-relativistic frame is reduced by a factor $\sqrt{1+f_B^2}$ compared to the standard non-relativistic phase speed when the Alfvén speed is not small compared to c. The reason for this decrease in the phase speed is related to the increase of the effective inertia of the fluid [as apparent from the left hand side of the momentum equation (4.10)]; with higher inertia, the volume elements of the fluid require a larger force to be accelerated, resisting changes in motion.

This has important consequences also in terms of the limitation of the timestep in numerical calculations. From the Courant-Friedrichs-Lewy condition one can obtain: $\Delta t = f_{CFL}\Delta x/u_{max}$ with $u_{max} = \max(|v+v_{ph}|, |v-v_{ph}|)$. For cases with relativistic Alfvén speed:

$$\Delta t \approx \frac{f_{CFL}\,\Delta x}{v_A}\sqrt{1+f_B^2}\,. \tag{4.17}$$

This is why the semi-relativistic approach is used in some numerical models of the solar corona in our days ([Rempel 2016], [Chen et al. 2022]).

For adiabatic perturbations, the amplitude relations are: $\frac{\rho'}{\rho_{eq}} = \frac{1}{\gamma}\frac{p'}{p_{eq}} = \pm\frac{v'}{v_{ph}} = \pm\frac{v'}{(c_{ms})_{eq}}\sqrt{1+f_B^2}$. For equilibrium states with the same $(c_{ms})_{eq}$, the perturbation amplitude will be greater if the Alfvén speed is relativistic.

4.1.3 Semi-relativistic shocks

For semi-relativistic shocks, in contrast to Sections 2.1.3 and 3.1.3, jump relations cannot be determined analytically, nor can they be found in the literature. Then, the step-functions that we used to define the initial situation with pre and postshock values to each side are no longer feasible. The postshock values will not adapt to the exact values that the shock would take, and there will be extra perturbations across it. Instead, we will solve the *Riemann problem* [Toro 2009]. This is a widely used situation in fluid dynamics and MHD simulations, consisting in an initial state characterised by a discontinuity. There is an analytical solution to predict the evolution in the simplest cases of non-relativistic speeds. In the simplest case, there will be a shock wave propagating to one side of the discontinuity, a rarefaction wave propagating in the opposite direction on the other side, and a contact discontinuity in the postshock medium. In this case of semi-relativistic shocks the jump relations and shock front speed are unknown and can only be estimated via the numerical experiments.

4.2 The Boris correction

The Boris correction [Boris 1970] is a modification that limits the signal propagation velocities of a MHD fluid, reducing the computational timestep and permitting longer evolution times in simulations. This correction is based on artificially lowering the speed of light, which will increase the value of the f_B parameter, reducing the signal propagation velocity (4.16) in the problem. This change can have important consequences for the numerical calculation of the solutions of the system, since Δt increases with increasing f_B for explicit numerical schemes, as seen in (4.17).

When the system one is studying naturally reaches a steady state, the Boris correction can accelerate the numerical calculation of the process, as explained by Gombosi et al. 2002. In a steady state situation, the semi-relativistic terms that contain the speed of light disappear because time derivatives cancel. Nevertheless, Rempel 2016, Chen et al. 2022 and other authors use this correction in calculations of non-stationary time evolution. It is even used in explosive situations like modeling of flares with values of $f_B > 1$ [Cheung et al. 2019]. So, it is of interest to explore some of the consequences of the correction in time-dependent calculations.

An example of the effect of this correction is the following: if one has a given $v_A \ll c$, an artificial value of $c = 1.5\, v_A$ can be set, i.e., $f_B = 2/3$, and the new phase speed will be $v_{ph} = c_{ms}/\sqrt{1 + 1/1.5^2} = c_{ms}/1.2$. The time step has increased by 20%, making calculations faster.

4.3 Numerical solution

The semi-relativistic calculations will be solved through the *Lax-Wendroff* scheme with the *Von-Neumann* artificial viscosity. The difference with the previous cases will be how the numerical densities and fluxes are calculated. The mass, momentum and energy volumetric densities for the numerical calculation and the equivalent numerical quantity for the magnetic field can be written now:

$$u_m = \rho \ , \quad u_B = B \ , \quad u_c = \rho\, v \left(1 + f_B^2\right) \quad u_e = \frac{p}{\gamma - 1} + \rho \frac{v^2}{2} \left(1 + f_B^2\right) + \frac{B^2}{2\mu_0} \ . \tag{4.18}$$

On the other hand, the mass, momentum and energy fluxes and the equivalent quantity for the magnetic field are left as:

$$f_m = \rho\, v \ , \tag{4.19}$$

$$f_B = B\, v \ , \tag{4.20}$$

$$f_c = \rho\, v^2 \left(1 + \frac{1}{2} f_B^2\right) + p + \frac{B^2}{2\mu_0} \ , \tag{4.21}$$

$$f_e = \left(\rho \frac{v^2}{2} + \frac{\gamma}{\gamma - 1} p + \frac{B^2}{\mu_0}\right) v \ . \tag{4.22}$$

4.4 Results

4.4.1 Semi-relativistic magnetosonic wave test

As explained in Section 4.1.2, if a small perturbation is added to the equilibrium state as the initial condition, the perturbation will propagate with phase speed v_{ph} given by (4.16). As now these propagation speeds can no longer be well below the artificially reduced speed of light when f_B is not small, but we have considered that the physical fluid velocities v are non-relativistic, we cannot jump onto the reference system that moves with v_{ph} because then the fluid elements would have relativistic velocities. Instead, we chose $v_{eq} = 0$ and the numerical perturbation propagation speed will be monitored by tracking the position of a point of the perturbation and the time elapsed.

For the numerical test, we defined an equilibrium state: $p_{eq} = 1.15$, $\rho_{eq} = 0.8$, $v_{eq} = 0$ and $B_{eq}/\sqrt{\mu_0}$ varied so that β_{eq} went from 0.1 to 10. We added a small amplitude perturbation with the shape of a cosine with wavelength $\lambda = 10$, and measured the propagation speed by tracking the maximum of the perturbation as it propagated. Following by the Boris correction, the speed of light was artificially varied so that the Boris factor $f_B = v_A/c$ went from 0 to 1 for each β_{eq}. A video animation of the $f_B = 0.5$ case with $\beta_0 = 0.1$ can be seen here. For each case, the measured phase speed, velocity perturbation amplitude v', time step Δt and number

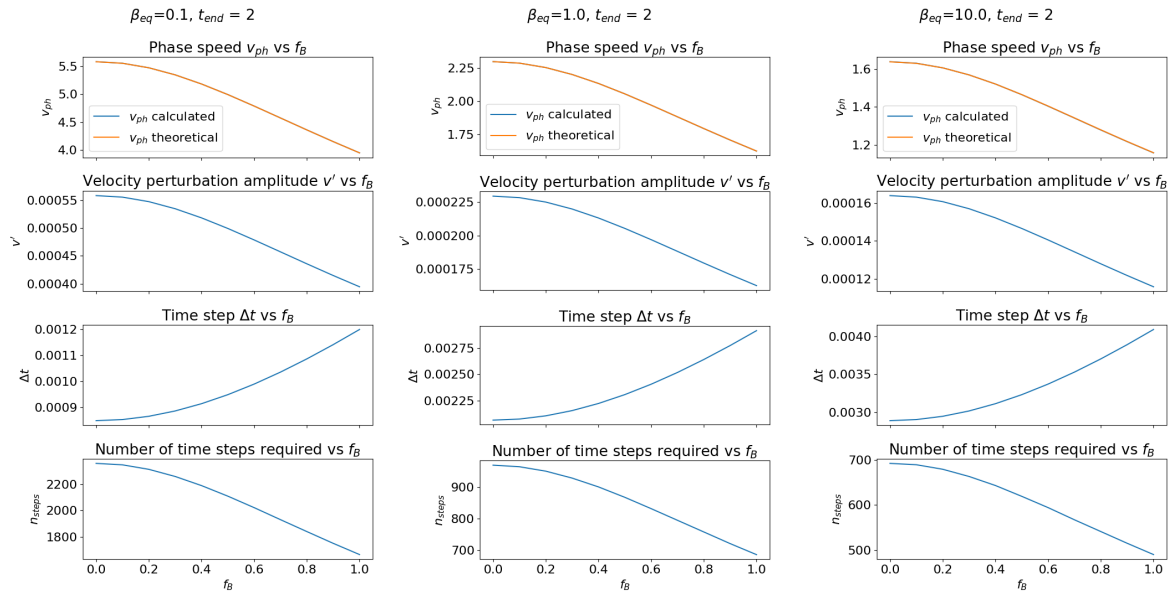

(a) $\beta_{eq} = 0.1$ (b) $\beta_{eq} = 1$ (c) $\beta_{eq} = 10$

Figure 7: Variation of phase speed (upper row of panels), velocity perturbation amplitude (upper middle row), timestep length (lower middle row) and number of required timesteps (lower row) as a function of f_B, calculated for $\beta_{eq} = 0.1$ (left column), $\beta_{eq} = 1$ (middle column) and $\beta_{eq} = 10$ (right column). For the phase speed, the numerical value (blue curve) is compared to the theoretical value given by (4.16) (orange value); the match between the two is very good, so that only one of them is visible in the figure.

of time steps required to reach $t_{end} = 2$ were recorded. The results are plotted in Figure 7. For the phase speed, the numerically calculated value (blue curve) is compared with the expected theoretical value (orange curve) given by equation (4.16). The blue line precisely matches the orange line and is hidden behind it. The perturbation amplitude profile has exactly the same shape as the phase speed profile as it fulfills $\frac{\rho'}{\rho_{eq}} = \frac{1}{\gamma}\frac{p'}{p_{eq}} = \pm\frac{v'}{v_{ph}} = 10^{-4}$, so their quotient has to be constant. As f_B grows from 0 to 1, both the perturbation amplitude and the phase speed decrease to 70% of their initial value. Consequently, the length of the time step increases by $(100/0.7)\% = 143\%$, while the number of time steps required to reach the final time decreases to 70% of their initial value.

This simple test proves that the propagation speed varies when changing artificially the value of the speed of light, and that the numerical calculations of the program work correctly.

4.4.2 Semi-relativistic MHD shock test

The absence of a complete semi-relativistic MHD shock theory, as commented in Section 4.1.3, leads us to study the evolution of the shock and the dependence on the Boris factor f_B by

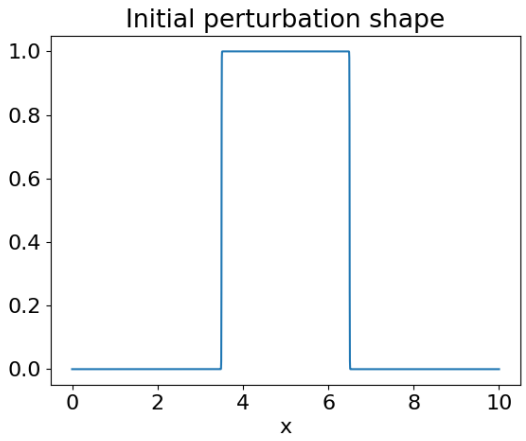

Figure 8: Initial perturbation profile for the Riemann problem, created with hyperbolic tangents.

analyzing Riemann problem situations. We experimented with an initial situation in the shape of a column perturbation as shown in Figure 8, with, however, the vertical walls turned into hyperbolic tangents to prevent the singular behaviour of the numerical solution from time 0. To simulate a situation in which an explosive phenomenon is taking place in the Sun, the perturbation is applied only in the gas pressure and magnetic field profiles, having instead a flat profile for the initial density and relative velocity. Then, there will be two shock waves running outwards, away from the initial column; also, two rarefaction waves propagating inwards, away from the discontinuities. If we label with A the amplitude of the column jump for the gas pressure, then we choose the jump for the magnetic field to be $\sqrt{A}$, so that the total pressure has a jump of A.

We start by testing how the code behaves when solving a standard MHD Riemann problem with no Boris correction, i.e., when $f_B = 0$. Figure 9 illustrates the results. It uses a column perturbation with amplitude $A = 20$ for the gas pressure and $\sqrt{20}$ for the magnetic field, creating a jump of value 20 in the total pressure. For this case, $\beta_0 = 0.1$.
It can be clearly appreciated that there are two shock waves propagating outwards of the central region, characterized by the steep increase of density, velocity or total pressure. The shock front speed is measured by detecting and storing its position every hundred time steps and carrying out a linear fit. The postshock values of the physical quantities are measured by taking the average value of the region between the shock front and the contact discontinuity, and, in the figure, are marked with horizontal lines. In the domain between the shocks and not far from them there is a contact discontinuity, which is also a standard feature of the solution of the Riemann problem and is apparent in every profile except those for the total pressure and velocity plots. A striking detail of this perturbation is the noise, clearly seen in the density, gas pressure and magnetic field profiles, and consequently in the plasma beta profile too. The artificial viscosity

previously included does not fix this noise because it is only applied when $dv/dx < 0$, and in the contact discontinuity the velocity profile is flat, so a different approach to reduce it is required.

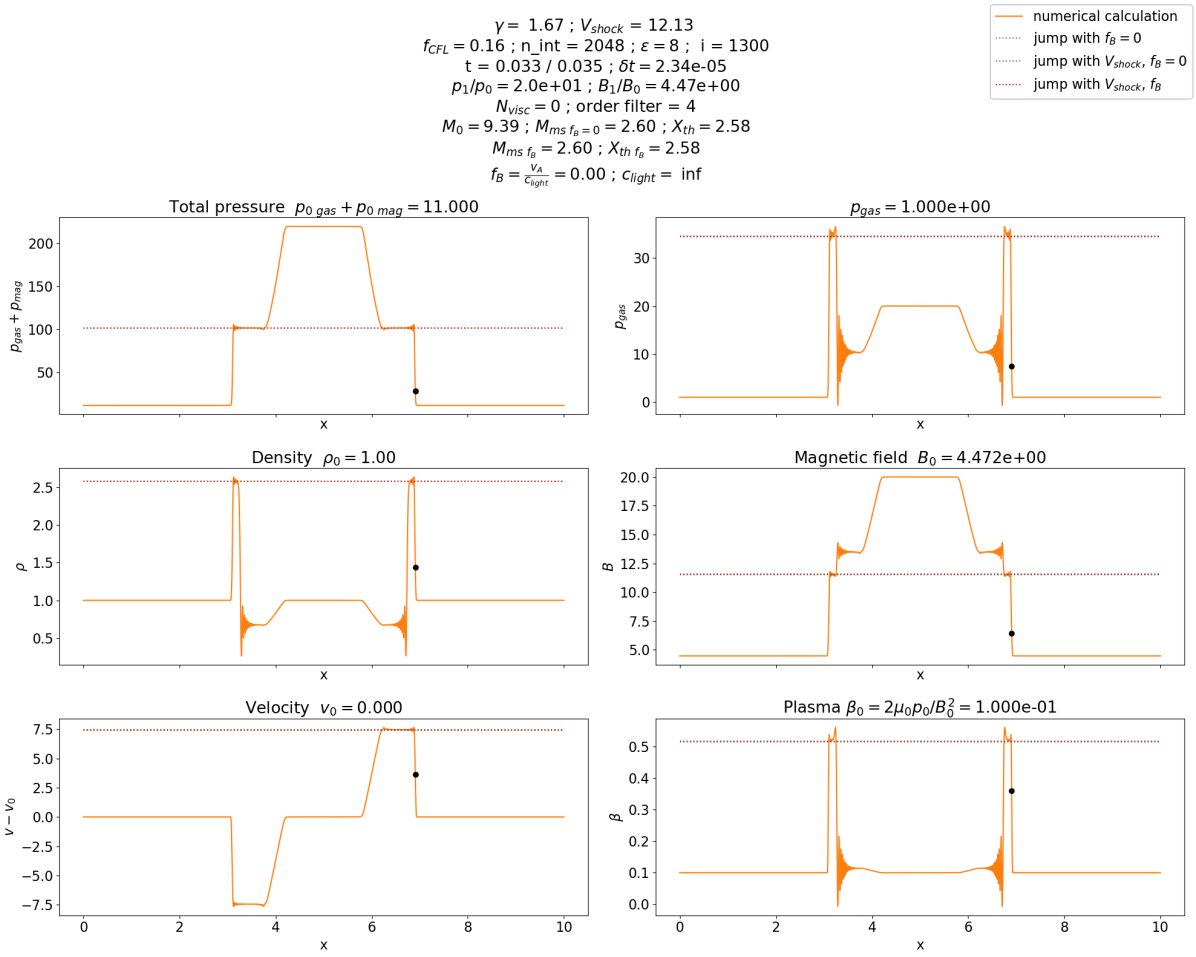

Figure 9: Time evolution up to $t = 0.035$ of the Riemann problem with initial column discontinuity with width 3 and height 20 in gas pressure and $\sqrt{20}$ in magnetic field. For this case $f_B = 0$ so after V_{sh} is numerically determined, horizontal lines are used to mark jump calculations for all physical quantities. The black dot indicates the shock position that is used to calculate V_{sh}.

We implemented a 4^{th} order filtering method to eliminate this high spatial frequency signal.

$$u_i = \frac{5}{8}u_i + \frac{1}{4}(u_{i-1} + u_{i+1}) - \frac{1}{16}(u_{i-2} + u_{i+2}) \tag{4.23}$$

It involves two points on each side of the central point, and is applied at each iteration. We have checked that this kind of filter does not affect the postshock values or any propagation speed, nor does it weaken relevant perturbation properties (the sum of all coefficients is 1, so the conservation law is still fulfilled). The filter was used for the simple classical and non-relativistic cases and compared to the analytical solutions, accurately calculating all properties. Figure 10 is a proof of the effect of using the filter. It can be seen that the noise has disappeared while the shape of all profiles has not changed.

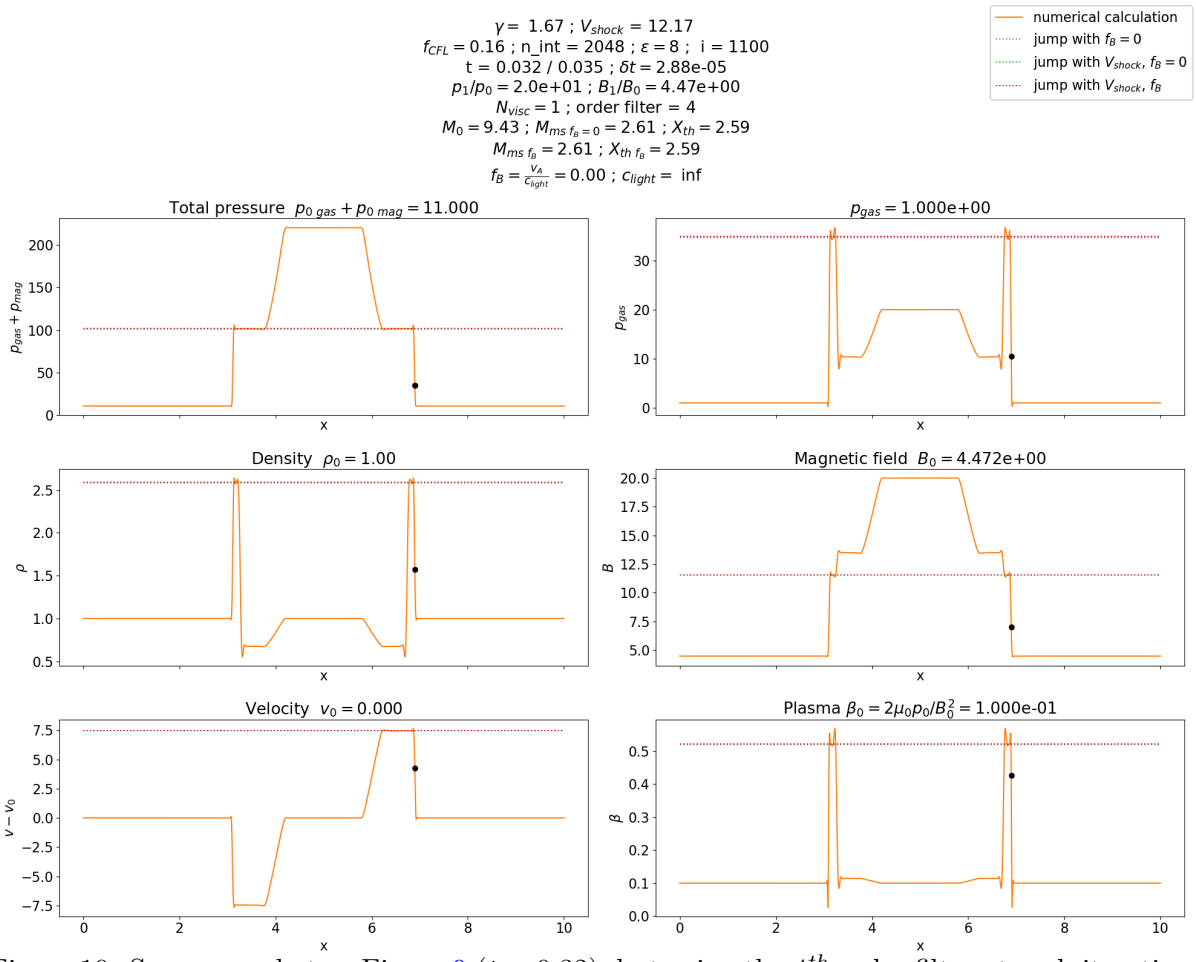

Figure 10: Same snapshot as Figure 9 ($t = 0.32$), but using the 4^{th} order filter at each iteration. The noise has disappeared, while all profiles keep their shape. A video animation of this case can be seen here.

Once the ability of the code to solve the Riemann problem for an explosion-like situation is proved for the non-relativistic case ($f_B = 0$ in previous examples), the Boris correction can be investigated in shocks. As there are no known jump relations or analytical values, the dependence of different parameters with respect to f_B will be studied. The simulation will be evolved to a more advanced physical time than the one used for the $f_B = 0$ case of Figure 10, so that there is a larger separation in space between the shock front and the contact discontinuity, as shown in Figure 11.

The experiment is carried out for β_0 equal to 0.1, 1 and 10, and for each case it is repeated reducing artificially the speed of light so that f_B goes from 0 to 1. Rempel 2016 and Chen et al. 2022 use values of f_B greater than 1 in their work, but we will limit ourselves to f_B between 0 and 1 in this thesis to avoid extreme cases.

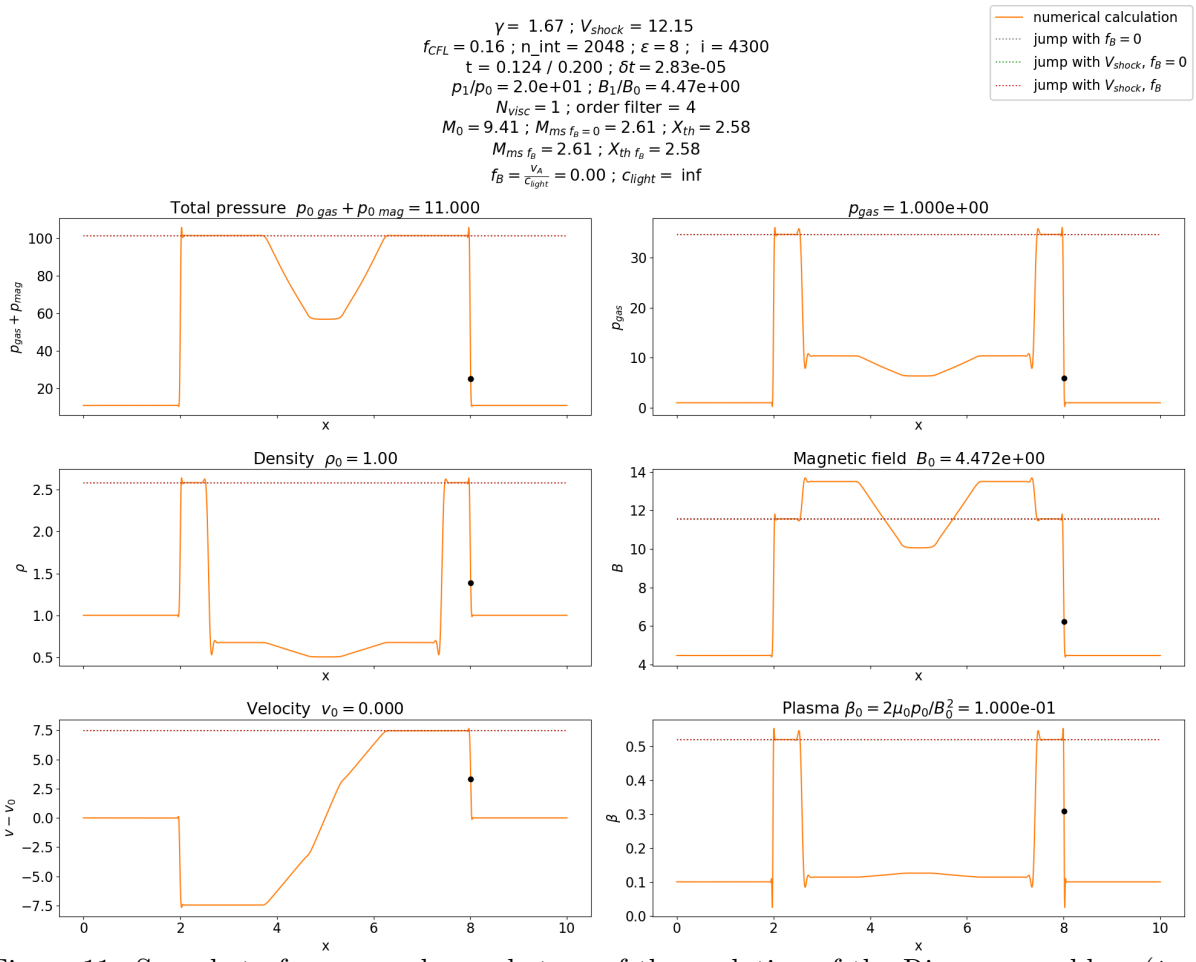

Figure 11: Snapshot of a more advanced stage of the evolution of the Riemann problem ($t = 0.124$) for $f_B = 0$, $\beta_0 = 0.1$ and using the 4^{th} order filter used at each iteration. A video animation of this case can be seen here.

We have created a system with initial values $p_0 = 1$, $\rho_0 = 1$, $v_0 = 0$ and $B_0 = 1$, and a column perturbation of jump 20 in gas pressure and magnetic field. We have let the system evolve for various f_B values, solving the Riemann problem and focusing on the resulting shocks. The main aspect we study is how the properties of the shocks vary between cases with different f_B. A secondary aspect is contemplated by measuring the jumps across the shock for a given f_B and comparing its properties (M_0, $M_{0\,ms}$, jumps, etc) to those of a shock with the same propagation speed but assuming $f_B = 0$, as there is an analytical solution for the latter case (as was explained in Section 3.1.3). A video animation of this experiment with $\beta_0 = 0.1$ and $f_B = 0.5$ can be seen here.

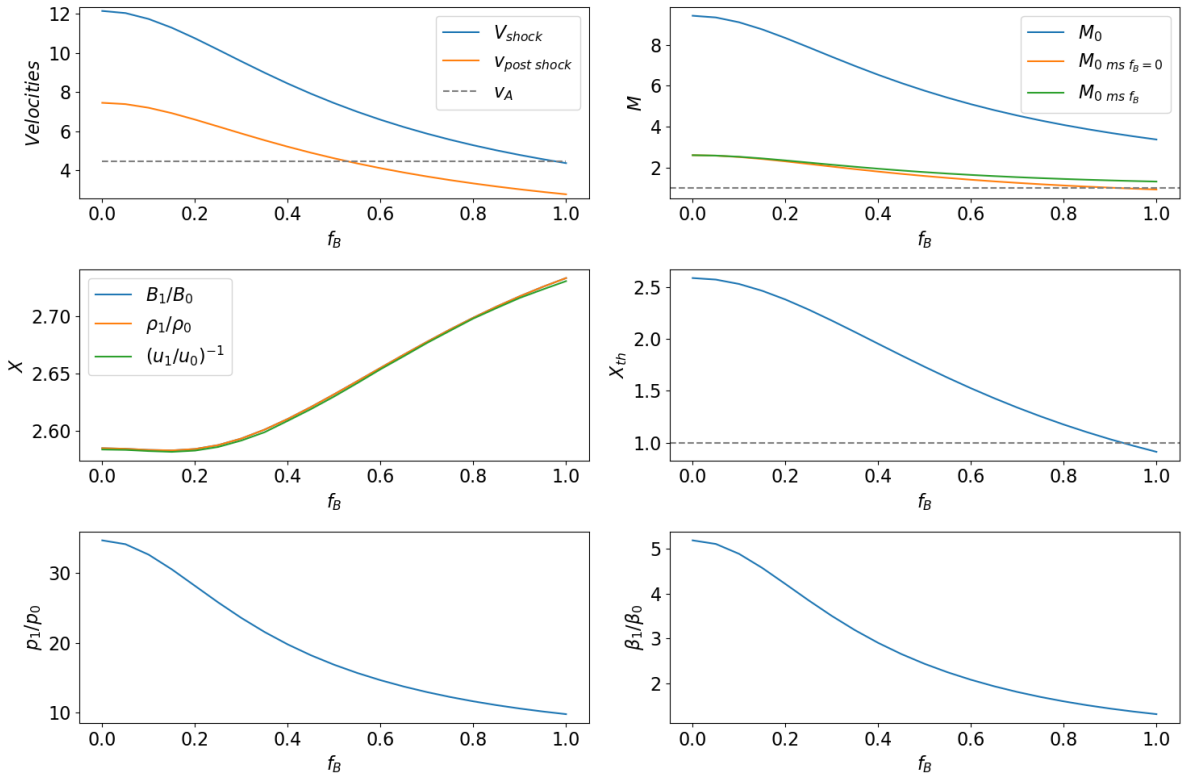

Figure 12: Jump variations depending on f_B for $\beta_0 = 0.1$. The upper row contains the shock front and postshock speed variations in the left panel and the Mach number variation in the right panel. The middle row contains the numerically measured jump in the left hand panel and the theoretically calculated jump using non-relativistic MHD theory. The bottom row contains pressure jump in the left hand side and plasma beta jump in the right hand side.

These tests are shown in Figures 12, 13 and 14, which correspond to cases of low, medium and high plasma beta. The top-left panel depicts the change of the shock front speed and the postshock speed as a function of f_B. A horizontal grey line represents the Alfvén speed. For the case of $f_B = 1$, c will be equal to it. It can be seen that both V_{sh} and $v_{post\ shock}$ decrease by roughly a factor of 2 when f_B increases from 0 to 1 in all the different β_0 cases.

The top-right panel depicts the variation of Mach numbers as a function of f_B. The sonic Mach number $M_0 = |u_0|/c_{s0}$ (blue curve) is expressed as V_{sh}/c_{s0} because $v_0 = 0$. The orange line represents the magnetosonic Mach number that would be obtained for a shock with the same propagation speed but in a non-relativistic situation $f_B = 0$, i.e., $M_{0\,ms\,f_B=0} = V_{sh}/c_{ms\,0}$. The green line represents the magnetosonic Mach number obtained when c_{ms} is calculated using the semi-relativistic expression (4.16), i.e., $M_{0\,ms\,f_B} = V_{sh}\sqrt{1+f_B^2}/c_{ms\,0}$. It can be seen that they all decrease with f_B, as V_{sh} decreases while the sound speed or magnetosonic speed are constant. Nevertheless, the expression for $M_{0\,ms\,f_B}$ has V_{sh} multiplied with the square root factor that increases when f_B grows. This ensures that it does not go below the dashed

grey line at 1. It indicates that the perturbation is still a shock, i.e., its propagation speed is faster than the propagation speed of magnetosonic waves in this semi-relativistic context.

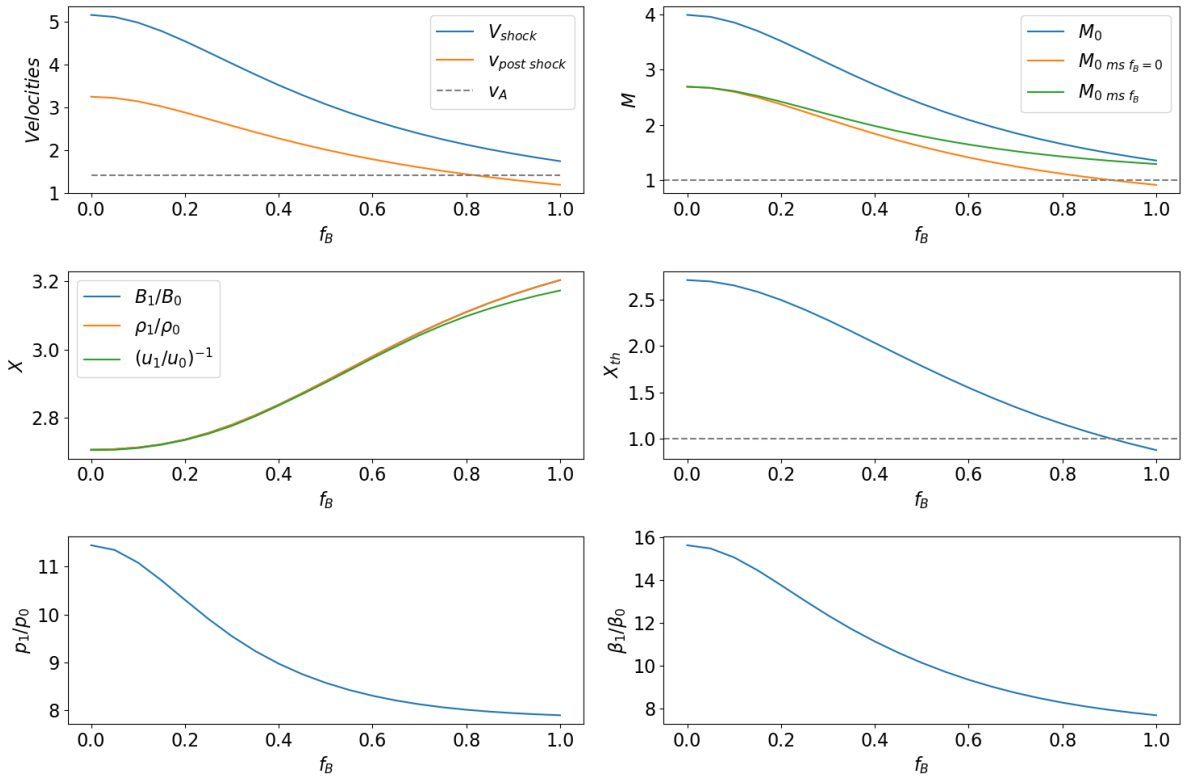

Figure 13: Jump variations depending on f_B for $\beta_0 = 1$. The panels represent the same physical quantities as Figure 12.

The second row focuses onto the jump coefficient X. The left side panel depicts the value one can obtain for it using the expressions (3.29-3.31) with the experimentally measured jumps for B_1/B_0, ρ_1/ρ_0 and u_0/u_1. For the low plasma beta case, it does not vary more than 10%, for the unity plasma beta case it varies about 20% and for the high plasma beta case, varies about 30%. In all cases the variation is an increase with similar shape.

The right hand panel of the second row shows the theoretical jump coefficient X that would be obtained by finding the positive root of (3.33). The parameter X depends on M_0, β_0 and γ, so the line is obtained by introducing the sonic Mach number M_0 numerically calculated for each f_B in that equation. It decreases to even below 1 with the same behaviour for every β_0, contrary to what the experimental jump coefficient does. The magnetosonic expression (3.33) does not hold at all in this context.

The bottom row shows the gas pressure and β jumps. Gas pressure behaviour varies for each β_0 case. For medium and low plasma beta situations it drops as f_B increases, while for the high plasma beta case it drops initially but then increases. The β jump profile, on the other hand, has similar behaviour in all cases.

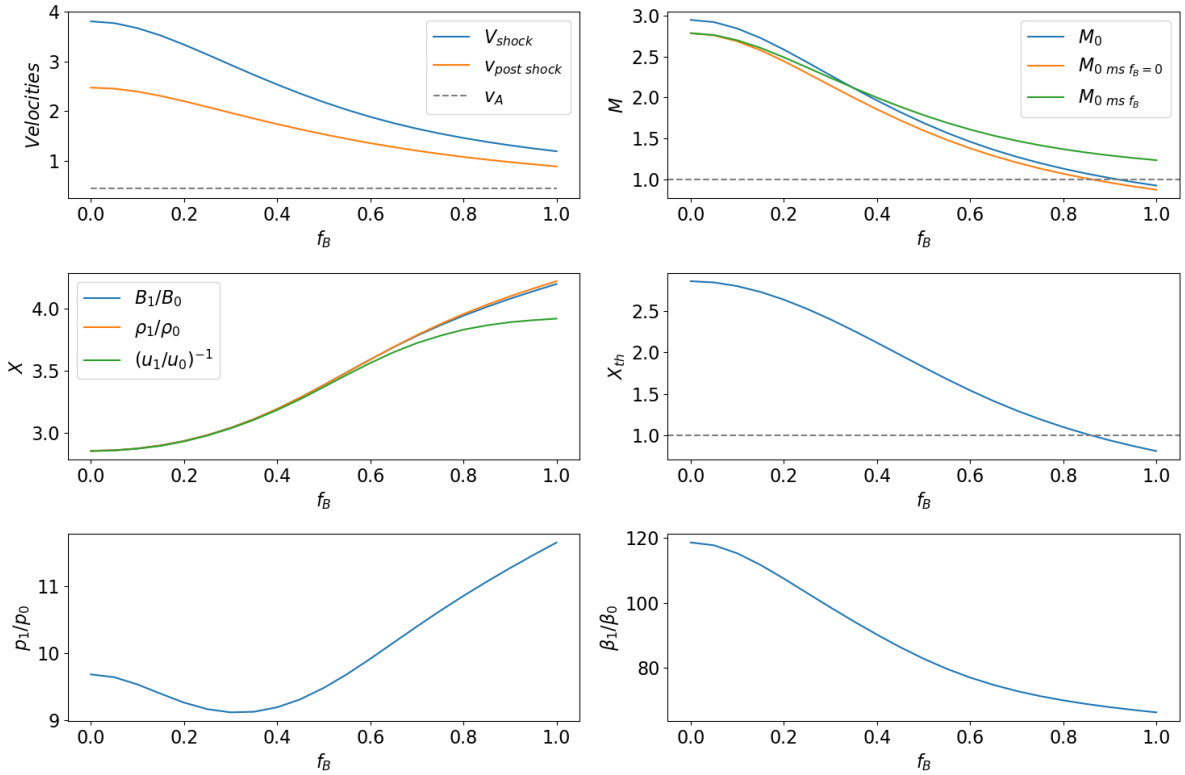

Figure 14: Jump variations depending on f_B for $\beta_0 = 10$. The panels represent the same physical quantities as Figure 12 and 13.

Summarising the results just obtained, we have seen that when f_B increases, the shock front speed markedly decreases for high, medium or low initial plasma β_0 values. For values of f_B close to 1 (which are lower than those used in the recent astrophysical literature mentioned along this chapter), the value of the shock speed is some 36% (for $\beta_0 = 0.1$), 34% (for $\beta_0 = 1$), and 31% (for $\beta_0 = 10$) of the standard MHD value for $f_B = 0$. The resulting shocks have values for the fundamental jump quantity X which are larger by factors 1.06 (for $\beta_0 = 0.1$), 1.18 (for $\beta_0 = 1$) and 1.48 (for $\beta_0 = 10$) for $f_B = 1$ compared to the standard MHD value (i.e., for $f_B = 0$). We conclude that the properties of the shocks within the Boris correction are noticeably different to those of the standard MHD theory.

5 Conclusions

En el capítulo actual se presentan las conclusiones del Trabajo de Fin de Grado. Se considera que se ha desarrollado una herramienta sencilla que permite comprender el efecto de la corrección de Boris en el caso específico unidimensional de campo magnético perpendicular a la velocidad del fluido. Se concluye que esta técnica altera importantemente las características de los choques. Un análisis profundo de las implicaciones de estos resultados escapan de los objetivos del presente Trabajo de Fin de Grado, pero puede ser estudiado en el futuro.

In this Graduation Thesis, we have created a code from scratch capable of solving the general equations of magnetohydrodynamics in one dimension for the case of longitudinal velocity and transverse magnetic field. The code was extended to cope with the set of semi-relativistic equations used in the Boris correction.

The effectiveness of the code has been thoroughly tested. The simplest hydrodynamic simulations matched analytical results. Sound wave amplitude and phase speed were accurately calculated, just as shock jumps and shock front speeds. This was checked using two different numerical schemes, and it was verified that the Lax-Friedrichs scheme is robust but rather dissipative, whereas the Lax-Wendroff MacCormack one had low dissipation. The latter code was therefore selected for the rest of the experiments. The Ritchmeyer-Von-Neumann artificial viscosity also proved its ability to reduce inconvenient ripples formed in shock fronts. The code was validated against simple magnetohydrodynamic waves and shocks as well, accurately calculating wave amplitude, phase speed, shock jumps and shock front propagation speeds under the assumptions of charge neutrality, infinite conductivity and non-relativistic speeds.

With a view to testing the Boris correction, the semi-relativistic MHD equations have been considered, i.e., the combination of non-relativistic fluid dynamics and Maxwell's equations including the displacement current. The code was tested and shown to calculate correctly the propagation of magnetosonic waves in that context. Following the guidelines of the Boris correction, the Boris factor $f_B = v_A/c$ was artificially increased in the range (0,1). As there is no theoretical, exact formulae for shocks in this situation, we have analyzed the shock propagation speed and jump values across it starting with a pressure pulse of column shape. From the tests, we conclude that the application of the Boris correction leads to a marked reduction of the shock front velocity, while the jump coefficient X increases appreciably. This behaviour leads to shocks that cannot be predicted by the standard MHD theory. We conclude that the Boris correction is able to reduce the time-step as expected, but also changes in important ways the

time evolution of the system, at least in explosive situations.

The code developed in this Graduation Thesis can be generally used for 1D problems in non-relativistic contexts and in that sense it can be useful to pursue a large range of problems. Here we have enlarged it to carry out a test of the Boris correction. A deeper analysis of the implications of our results concerning this correction goes beyond the scope of the present Graduation Thesis and may be pursued in future studies.

References

Boris, JP (1970). *A physically motivated solution of the Alfvén problem*. Tech. rep. NAVAL RESEARCH LAB WASHINGTON DC.

Boyd, TJM and Sanderson, JJ (2003). *The Physics of Plasmas*. Cambridge University Press. DOI: 10.1017/CBO9780511755750.

Chen, F, Rempel, M, and Fan, Y (2022). "A Comprehensive Radiative Magnetohydrodynamics Simulation of Active Region Scale Flux Emergence from the Convection Zone to the Corona". In: *The Astrophysical Journal* 937, p. 91. DOI: 10.3847/1538-4357/ac8f95.

Cheung, MCM, Rempel, M, Chintzoglou, G, Chen, F, Testa, P, Martínez-Sykora, J, Sainz Dalda, A, DeRosa, ML, Malanushenko, A, Hansteen, V, De Pontieu, B, Carlsson, M, Gudiksen, B, and McIntosh, SW (2019). "A comprehensive three-dimensional radiative magnetohydrodynamic simulation of a solar flare". In: *Nature Astronomy* 3, pp. 160–166. DOI: 10.1038/s41550-018-0629-3.

Courant, R, Friedrichs, K, and Lewy, H (1967). "On the Partial Difference Equations of Mathematical Physics". In: *IBM Journal of Research and Development* 11, pp. 215–234. DOI: 10.1147/rd.112.0215.

Gombosi, T, Tóth, G, Zeeuw, D, Hansen, K, Kabin, K, and Powell, K (2002). "Semirelativistic Magnetohydrodynamics and Physics-Based Convergence Acceleration". In: *Journal of Computational Physics* 177, pp. 176–205. DOI: 10.1006/jcph.2002.7009.

Laney, CB (1998). *Computational Gasdynamics*. Cambridge University Press. DOI: 10.1017/CBO9780511605604.

Priest, E (2014). *Magnetohydrodynamics of the Sun*. Cambridge University Press. Chap. Chapter 5.3. DOI: 10.1017/CBO9781139020732.

Rempel, M (2016). "Extension of the MURAM Radiative MHD Code for Coronal Simulations". In: *The Astrophysical Journal* 834.1, p. 10. DOI: 10.3847/1538-4357/834/1/10.

Toro, E (2009). *Riemann Solvers and Numerical Methods for Fluid Dynamics: A Practical Introduction*. Springer. URL: https://books.google.es/books?id=SqEjX0um8o0C.